Surface & Coatings Technology 494 (2024) 131353

Contents lists available at ScienceDirect

Surface & Coatings Technology

journal homepage: www.elsevier.com/locate/surfcoat

Effect of laser energy on the fretting wear resistance of femtosecond laser shock peened Ti6Al4V

Xuan Huang [a,b,c], Kai Chen [c,*], Liucheng Zhou [d,*], R. Lakshmi Narayan [e], Upadrasta Ramamurty [f]

[a] National Key Lab of Aerospace Power System and Plasma Technology, Xi'an Jiaotong University, Xi'an 710049, P.R. China
[b] School of Mechanical Engineering, Xi'an Jiaotong University, Xi'an 710049, P.R. China
[c] Center for Advancing Materials Performance from the Nanoscale (CAMP-Nano), State Key Laboratory for Mechanical Behavior of Materials, Xi'an Jiaotong University, Xi'an, Shaanxi 710049, P.R. China
[d] Science and Technology on Plasma Dynamics Laboratory, Air Force Engineering University, Xi'an, Shaanxi 710038, P.R. China
[e] Department of Materials Science and Engineering, Indian Institute of Technology, Delhi, New Delhi 110016, India
[f] School of Mechanical and Aerospace Engineering, Nanyang Technological University, Singapore 639798, Singapore

ARTICLE INFO

Keywords:
Femtosecond laser shock peening
Laser energy
Laser-induced periodic surface structures
Fretting wear resistance
Plastic deformation
Gradient structure

ABSTRACT

Femtosecond laser shock peening (FsLSP) is performed on engineering alloys to improve their wear resistance in dry and oil-lubricated sliding conditions. In this study, the influence of FsLSP on the fretting wear behavior of Ti6Al4V alloy is studied. For this purpose, FsLSP treatment, with laser energies of 50, 100, 150, and 200 μJ, is performed on a Ti6Al4V sample which mainly consists of α-phase. Topographical investigations using white light interferometry reveal that with increase in the laser energy, the coverage area of laser-induced periodic surface structures (LIPSSs) decreases, and the extent of surface pitting damage increases, leading to higher surface roughness. While surface hardness also initially increases with increasing laser energy, it remains invariant when the energy is increased beyond 150 μJ. Sub-surface microstructural investigations and kernel average misorientation maps obtained from electron backscatter diffraction reveal that FsLSP treatment leads to the formation of severely deformed and mildly deformed layers along the depth of the alloy surface. Surface hardening due to FsLSP is attributed to the activation of prismatic <a>, basal <a> slip systems, and $\{1\,0\,\bar{1}\,2\}$, $\{1\,1\,\bar{2}\,3\}$ tensile twins in the severely deformed zone along with grain refinement, which is an outcome of dynamic recrystallization. Fretting wear tests indicate that the coefficient of friction (CoF) of FsLSP treated alloys is consistently lesser than that of its as-received counterpart, whose CoF is 0.38. In contrast, the wear resistance, quantified by the wear rate, wear volume and wear depth, is highest in the sample treated with laser energy of 100 μJ but lower for the as-received as well as 150 and 200 μJ laser treated samples. These results are explained on the basis of the differences in the contact area, formation of surface hardening layer and the size and integrity of asperities on the surface, which in turn influences the dominant fretting wear mechanism.

1. Introduction

The titanium alloy, Ti-6Al-4V (Ti64), is extensively used for fabricating aeroengine components as it has high specific strength, superior intermediate temperature performance, and remarkable corrosion resistance [1,2]. One such critical component is the blade damping boss, which ensures the safe operation of the engine by absorbing the vibrational energy emitted by the turbine blades [3]. Since the blade damping boss is in close contact with the adjacent turbine blade during operation, it has a tendency to undergo micro-slip and fretting wear damage. Moreover, any fretting wear scars on the top surface of the boss act as a stress concentrator and promote the initiation of cracks, leading to its premature fracture, which, in turn, could lead to a catastrophic failure of the engine. Additionally, any wear-induced geometry changes in the boss surface can result in excessive blade vibrations, compromising the engine performance. To enhance the fretting wear resistance of Ti64, various surface strengthening methods such as the ultrasonic nanocrystalline surface modification, shot peening, and surface coatings have been explored [4–7]. Mechanical techniques, like shot peening, are particularly effective in increasing the wear resistance as they introduce compressive residual stress and work hardening on the surface. However, these methods often compromise the surface integrity, as they

* Corresponding authors.
E-mail addresses: kchenlbl@gmail.com (K. Chen), happyzlch@163.com (L. Zhou).

https://doi.org/10.1016/j.surfcoat.2024.131353
Received 4 June 2024; Received in revised form 6 September 2024; Accepted 9 September 2024
Available online 11 September 2024

increase its roughness that could compromise the fatigue performance by facilitating easy crack nucleation. While surface coatings such as Al-Bronze or Cu-Ni-In [8] may reduce the coefficient of friction (CoF), their relatively poor durability and weaker bonding strength with the underlying alloy limits their effectiveness. Therefore, neither shot peening nor surface coatings are ideal solutions for significantly enhancing the fretting wear resistance of components such as the blade damping boss.

A novel surface treatment, femtosecond laser shock peening (FsLSP), which employs femtosecond pulse lasers to irradiate metal surfaces in atmospheric conditions, has been developed in recent years to facilitate surface strengthening. This process generates shock waves, whose peak pressures range between 10^2 and 10^3 GPa [9], which deform the surface layers and induce residual compressive stresses within them [10–12]. Compared to nanosecond laser shock peening (NsLSP), which produces 1500 μm strain hardened layer, FsLSP introduces a layer that has a thickness of the order of a hundred micrometers [11,12]. A thinner hardened layer is favorable for surface treatment of relatively thin airplane components. This is because for components that have thickness < 6 mm, undergo considerable bending if the hardened surface layer is of the order of 1000 μm [13]. The effect of shot peening, NsLSP, and FsLSP on the roughness, residual stresses, hardened layer thickness and hardness of the surface of Ti64 are listed in Table 1.

Additionally, the ultra-short laser pulses interact with the metal surface to create laser-induced periodic surface structures (LIPSSs), which has a profound effect on the frictional properties of the metal [12,21–24]. For instance, Mizuno et al. [25] reported a decrease in the lateral force on the surface of diamond-like carbon films that contain LIPSS, when the normal loads are of the order of a few nN. Alternately, Eichstädt et al. [26] performed ball-on-disk tests at normal loads of the order of a few mN and concluded that the friction force on the surface of silicon is higher on a LIPSS covered surface compared to that of its untreated counterpart. For Ti alloys, Bonse and co-workers [22,24] performed reciprocating sliding wear tests on Ti64 covered with LIPSSs in oil-lubricated conditions and observed that the LIPSSs formed on the surface remained almost intact throughout the tests. They attributed the preservation of LIPSSs to the interaction between laser induced oxides on the surface of Ti64 with the anti-wear additive zinc dialkyl dithiophosphate, which is present in the engine oil, which forms a thin surface tribo-layer. This surface tribo-layer significantly reduces the CoF and improves the wear resistance of Ti64. Some studies [12] have also noted that the FsLSP treatment can enhance the wear resistance of Ti64 in dry sliding conditions, which was attributed to the introduction of LIPSSs, Ti oxide formation, and the presence of compressive residual stresses on the surface.

Although FsLSP has proven to be effective in enhancing the tribological performance of Ti alloys in both dry and oil-lubricated sliding wear conditions [12,22–24], its effectiveness in improving the fretting wear resistance has not been studied in detail. Fretting wear is distinct from dry sliding wear as it involves small amplitude displacements, of the order of micron to sub-millimeter scale, of an abrasive medium over the surface. Moreover, it could lead to crack initiation on the worn surface under cyclic stress. In contrast, sliding wear is characterized by material loss as the mating surfaces continuously slide over each other, which leads to surface material removal before crack initiation can occur. Therefore, understanding the effects of FsLSP treatment on the fretting wear resistance of Ti alloys is crucial for extending the service life of components like the blade damping boss. Fretting wear is closely associated with factors like frictional shear stresses, residual stresses, and surface roughness and texture [27,28]. Prior studies have shown that the surface microstructures of Ti64 alloy evolve from LIPSSs to groove and spike structures as the laser energy density increases [24]. Moreover, the surface roughness initially increases and then decreases as the laser energy increases [11]. Since laser energy has a significant influence on the surface morphology and roughness, it emerges as a vital parameter in assessing the influence of FsLSP treatment on the fretting wear resistance of Ti alloys.

With the motivation to explore the influence of FsLSP on the fretting wear resistance of Ti64, we performed fretting wear experiments on Ti64, which is treated with different femtosecond laser energies. Following detailed assessments of surface characteristics, material hardness, and performance in fretting wear tests, the most effective femtosecond laser energy is identified. The study also elucidates the mechanisms of fretting wear in both FsLSP treated and as-received samples and investigates the plastic deformation behavior along the shock wave propagation direction.

Table 1
Comparison of shot peening, NsLSP, and FsLSP on Ti alloy.

	Shot peening [7,14,15]	NsLSP [16–20]	FsLSP [12]
Surface roughness (μm)	1.7 ± 0.5	1.3 ± 0.2	1.2 ± 0.1
Surface residual stress (MPa)	−702.0 ± 138.6	−592.3 ± 65.3	−746.3 ± 7.4
Surface hardness (HV)	393.3 ± 40.1	381.7 ± 26.9	391.3 ± 14.6
Hardened layer thickness (μm)	112.5 ± 31.8	1550.0 ± 70.7	91.5 ± 12.0

2. Materials and methods

2.1. Materials

The 3 mm thick as-received Ti64 plate has a chemical composition (by weight) of 6.16 % Al, 3.95 % V, 0.03 % Fe, 0.04 % C, 0.06 % O, 0.014 % N, and 89.74 % Ti [11]. Prior to FsLSP treatment, it is ground and polished to a mirror finish, resulting in an areal average surface roughness, *Sa*, of around 0.15 μm, then cleaned in ethanol for 10 min.

2.2. FsLSP treatment

Four samples, with length, width, and thickness of 35, 15, and 3 mm, respectively, are sectioned from the Ti64 plate for performing the FsLSP treatment. A schematic illustration of the FsLSP process is shown in Fig. 1. In the same figure, a Cartesian coordinate system is included for reference. Fig. 1(a) illustrates the FsLSP setup, where the sample surface (*x*-*y* plane) is irradiated by a laser beam along *y* axis at a frequency of 50 kHz and scanning speed of 250 mm/s in standard atmospheric conditions, without the use of a sacrificial or confining layer. The laser has a pulse duration, spot diameter and wavelength of 290 fs, 20 μm and 1030 nm, respectively. A 5 μm gap between each adjacent scan is maintained. The four samples are treated with laser energies of 50, 100, 150, and 200 μJ. The corresponding laser fluences are 15.9, 31.8, 47.7 and 63.7 J/cm^2, respectively.

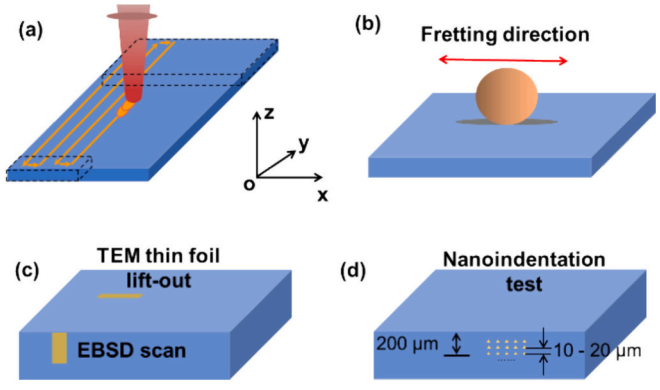

Fig. 1. Schematic illustration of (a) femtosecond LSP processing, (b) fretting wear tests, (c) TEM specimen preparations, EBSD characterization and (d) nanoindentation measurements.

2.3. Fretting wear tests

Tangential fretting wear tests, schematically illustrated in Fig. 1(b), are performed along the *x*-axis on the *x*-*y* plane of the as-received and FsLSP treated Ti64 samples, using a Si_3N_4 ball which has a diameter of 8 mm as the counterpart. The imposed normal load of 15 N and displacement amplitude of 100 μm are achieved by the weight and voice coil motor [29], respectively. Based on the Hertzian contact model of a ball (Si_3N_4) in contact with a flat surface (Ti64) [30,31], the average and maximum contact pressures are ~460 MPa and 689 MPa, respectively. To evaluate fretting regimes of different samples, the measured friction force and displacement of them are plotted as the hysteresis loops. Each sample is involved in 5×10^4 cycles at a frequency of 10 Hz to obtain the wear morphology, wear volume and wear rate. At least three tests are performed on each sample to ensure the repeatability of the experiments. All the fretting tests are conducted at room temperature in a dry condition under ambient atmosphere.

2.4. Materials characterization

The microstructure and morphology of FsLSP treated surface before and after performing the fretting wear tests were examined using a scanning electron microscope (SEM, Hitachi SU8230). A white light interferometer (Contour, Bruker), equipped with Vision software, is used for measuring the surface roughness, surface profile, wear scar profile, and wear volume.

Fig. 1(c) schematically illustrates the locations at which EBSD scans and TEM imaging are performed on the samples. For EBSD, a coupon is extracted from the *x*-*z* plane and scanned along the *z*-axis, with a step size of 0.1 μm, covering the top of the peened surface, and at locations beneath it up to a depth of 180 μm. Scanning is performed in an electron-ion dual beam system (Helios Nanolab 600), which has an electron-beam acceleration voltage of 20 kV and is equipped with an area detector to record the Kikuchi patterns. Data is acquired using the Aztec module (developed by Oxford Instruments) and then analyzed using an in-house developed software package XtalCAMP [32]. Thin foils were lifted out from the FsLSP treated surface, in the *x*-*y* plane, and imaged using a JEM-2100F transmission electron microscope (TEM).

Nanoindentation (TI950 nanoindenter), which is equipped with a Triboscanner control system and a Berkovich indenter, is used to obtain the surface hardness of the as-received and FsLSP treated Ti64 samples and the cross-sectional hardness of the 100 μJ sample. For the 100 μJ sample, nanoindentation measurements are performed along the *z*-axis on the *x*-*z* plane, as shown in Fig. 1(d). The imposed peak load is 5000 μN and the dwell time is 2 s. And the loading rate and unloading rate are both 1000 μN/s. Besides, the separation between two indentations along the z-axis is maintained at ~20 μm and at least five nanoindentation measurements are performed at each depth.

3. Results

3.1. Microstructural characterization of as-received Ti64

The phase maps obtained on the as-received Ti64 are displayed in Fig. 2(a). From this, it was determined that the volume fractions of α and β phases are 98.6 % and 1.4 %, respectively. Since α has a significantly higher volume fraction in the as-received alloy, it will be the primary focus of this study. A histogram of the α grain size distribution, shown in Fig. 2(b), reveals that the average α grain size is 2.43 ± 1.77 μm. Fig. 2 (c) and (d) show the corresponding inverse pole figure (IPF-Z) maps and pole figures of the as-received Ti64. Note that the *c*-axis of most of the α grains is parallel to the *y*-axis, their $\{10\bar{1}0\}$ plane normal is parallel to the *x*-axis and their $\{\bar{2}3\bar{1}8\}$ plane normal is parallel to the *z*-axis.

3.2. Surface morphology and hardness of as-received and FsLSP treated samples

Low and high magnification SEM images of the surfaces of all the four FsLSP treated samples are displayed in Fig. 3. In the 50 μJ sample (see Fig. 3(a1) and (a2)), while laser feeding traces are not visible on the surface at a low magnification, higher magnification images reveal the presence of LIPSSs, which have a period of ~0.3–0.5 μm. LIPSSs, whose period is considerably smaller than the wavelength of the incident laser beam, is referred to as high-spatial-frequency LIPSS (HSFL) [33]. While the formation mechanism of HSFL is still not well-established, it is likely to manifest from the interaction between the laser and surface scattered electromagnetic/surface plasmon polarization. The repetitive pattern of these HSFL is well described by a self-organization model [34,35]. As the laser increases, the LIPSSs become discontinuous and are interrupted by wavy trenches, which have a slightly darker contrast and are oriented roughly along the *x*-axis (see dotted lines in Fig. 3(a2-d2)). These trenches are also called micro-spaced grooves in the literature and are attributed to electromagnetic scattering, heat transfer and hydrodynamic effects originating from laser interaction with metal surface [36]. Additionally, some white particles are observed on the surface of the LIPSS, which are likely to be condensates of the alloy that evaporated and sublimated during the FsLSP process [37,38]. When the laser energy

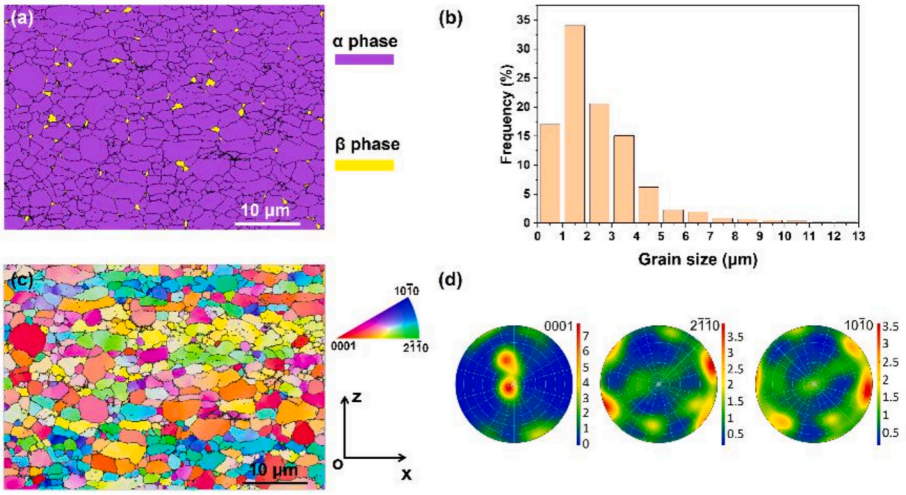

Fig. 2. EBSD maps of the as-received Ti64 plate: (a) phase map; (b) the histogram of α grain size distribution; (c) inverse pole figure (IPF) along the *z*-axis and (d) pole figure based on α phase.

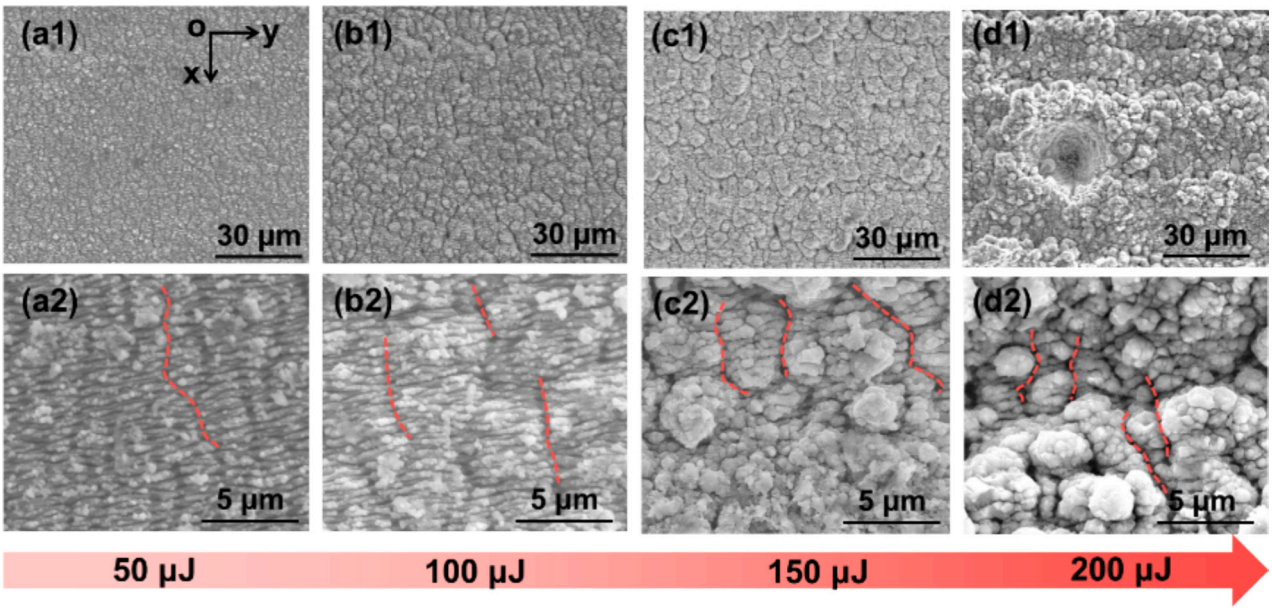

Fig. 3. Representative low and high magnification SEM images of samples treated with (a1)-(a2) 50, (b1)-(b2) 100, (c1)-(c2) 150 and (d1)-(d2) 200 μJ femtosecond laser, respectively.

is increased to 100 μJ (see Fig. 3(b1) and (b2)), the laser feeding traces on the surface become more prominent, the trenches become more distinct, and the size of the splashed white condensate particles increases. With further increase in the laser energy to 150 μJ (see Fig. 3 (c1)), the treated surface exhibits a fish-scale appearance owing to intensified ablation of the surface. Furthermore, a portion of the LIPSSs is obscured by large condensate particles that have dimensions of ~2 μm (see Fig. 3(c2)). In the 200 μJ sample, along with the laser feeding traces, pits that have a diameter of ~40 μm appear on the surface (see Fig. 3 (d1)). It is also evident that the area covered by LIPSSs diminishes and is instead overlaid with large irregular particles ((see Fig. 3(d2))). Such pits have also been observed in other studies involving FsLSP treatment on metals [36,39]. Pit formation is attributed to preferential valley ablation with increasing laser energy. During the initial stages of FsLSP treatment, trenches form on the surface of the alloy. However, since the intensity of fluence is significantly higher at higher laser energies, there is localized and concentrated ablation within the surface trenches which transform to these large pits.

Fig. 4(a) shows the surface profiles along the *x*-axis of the as-received and FsLSP treated samples. On all the treated sample surfaces, periodic undulations with distinct wavelengths and amplitudes are observed. The undulations on the sample exposed to laser energies of 50 μJ have a wavelength of ~8 μm, which is almost equal to the spacing between two adjacent laser scans. As the laser energy increases to 100 and 150 μJ, the undulation wavelength increases to ~12 μm, and the undulation wavelength of the 200 μJ sample is up to 20 μm, which is attributed to greater ablation of the surface. Similarly, there is a progressive increase in the amplitude of the undulations from 2.9 to 22.3 μm when the laser energy increases from 50 to 200 μJ. The surface roughness *Sa* of the as-received and FsLSP treated samples are shown in Fig. 4(b). While the surface roughness of the as-received sample is 0.15 ± 0.05 μm, that of the 50 and 100 μJ sample is two-fold higher. Further increase in the laser power to 150 and 200 μJ, increases the roughness to 1.50 ± 0.37 and 3.32 ± 0.91 μm, respectively. These trends suggest that increasing laser energy leads to greater ablation and plastic deformation of the surface.

To understand the effect of laser energy on the mechanical properties of the surface, the hardness, *H*, of the as-received and FsLSP-treated samples is assessed. Note that direct measurement of *H* by indenting

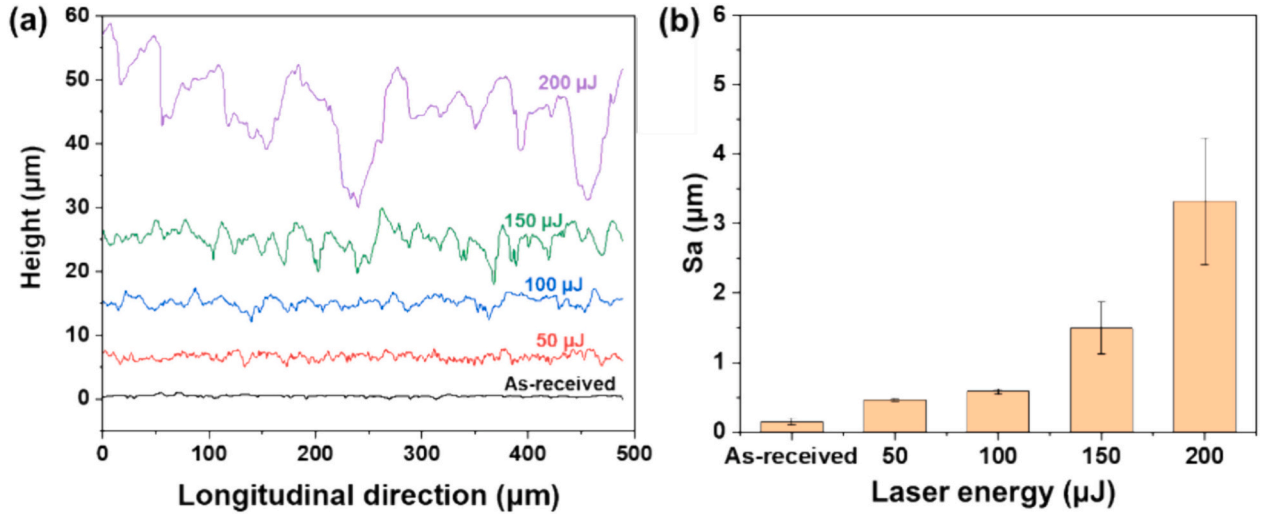

Fig. 4. (a) Surface profiles along the *x*-axis of different samples and (b) the corresponding surface roughness.

the FsLSP treated surfaces is impractical as their surface roughness interferes with the measurement of indentation diagonal lengths, which is of the order of a few μm. Alternately, nanoindentation tests are conducted on the *x-z* planes of as-received and FsLSP treated samples at a depth of 5 μm below the surface. Fig. 5(a) shows the plot of the measured H test data. While the H of the as-received sample is about 4.5 ± 0.2 GPa, that of 50 μJ sample is 4.6 ± 0.2 GPa, which is only marginally higher. For samples treated with higher laser energy, a steady increase in H is observed. For instance, H of the 100 and 150 μJ sample are 4.7 ± 0.3 and 5.0 ± 0.2 GPa, respectively. However, H of the 200 μJ sample is similar to that of the 150 μJ sample, which indicates that H does not increase further with increasing laser energy. Fig. 5(c) and (d) show the corresponding indentation modulus (E) and H^3/E^2 ratio [40,41] for all the samples. Note that H^3/E^2 is a measure of the resistance to plastic deformation. While the H^3/E^2 ratio of the as-received and 50 μJ samples are 0.0053 ± 0.0008 and 0.0054 ± 0.0006, it increases marginally to 0.0058 ± 0.0006 when the laser energies are increased to 100 μJ. However, further increase in laser energy leads to a dramatic increase in the H^3/E^2 ratio, which suggests that there is a significant increase in the surface resistance to plastic deformation.

3.3. Fretting wear behavior

The plots of the friction force and displacement as a function at different fretting cycles of the as-received and FsLSP treated samples are shown in Fig. 6. In the as-received sample, the height of the hysteresis loop increases abruptly after 50 cycles (see Fig. 6(a)), which indicates that the wear on the fretting surface gets aggravated. Beyond 900th cycles, the shape of hysteresis loop unchanged. In contrast, for the samples treated with 50, 100 and 150 μJ, there is a slow increase in the friction force in the first 900 cycles, and then starts increasing sharply after the 900th fretting cycle (see Fig. 6(b), (c) and (d)). For the sample treated with 200 μJ, the friction force increases continuously all the time and remains stable since the 3000th cycle (see Fig. 6(e)).

According to the hysteresis loops, the CoF of various specimens can be calculated by quadrupling the product of the normal load and theoretical displacement and then dividing by the area enclosed by the hysteresis loop in one fretting cycle [42]. The variations of CoF as a function of the number of fretting cycles, obtained from the fretting wear tests, on the as-received and FsLSP treated samples are shown in Fig. 7(a). A magnified portion of the curves, shown in Fig. 7(b), reveals that the variations in CoF can be categorized into three distinct stages, which are the initial, the escalation, and the dynamic equilibrium stages. In the initial stage, which encompasses the first 900 cycles, CoF increases with increasing number of cycles, in all samples. However, the rate of increase in CoF with the number of cycles is generally lower for the FsLSP treated samples compared to that of its as-received counterpart. In fact, CoF is roughly constant for the 50 μJ sample in the entire initial stage. However, for samples treated with higher laser energies, there is a steady increase in CoF. For instance, CoF increases from 0.125 to 0.225 in the 100 and 150 μJ samples, whereas it increases from 0.125 to 0.325 in the 200 μJ sample during the first 900 cycles. In contrast, within the same duration, CoF for the as-received sample increases from 0.10 to 0.40. These observations suggest that while FsLSP treatment limits the increase in CoF of the Ti64 surface, the rate of increase in CoF increases with the laser energy, in the initial stage of fretting.

During the escalation stage, which spans from the 900–3000 cycles, while CoF of the as-received sample is invariant, that of all the FsLSP treated samples increases further. Beyond 3000 cycles, in the dynamic equilibrium stage, CoF of the as-received and FsLSP treated samples remain broadly constant. The average CoF values of various samples are shown in Fig. 7(c). At this stage, CoF of the FsLSP treated samples is lower compared to that of the as-received sample counterparts. In fact, the 200 μJ sample exhibits a constant CoF of ~0.31 whereas that of the as-received sample is 0.38, which suggests that the FsLSP treatment improves the wear resistance of Ti64.

Worn morphologies of the as-received and treated samples after fretting wear test are shown in Fig. 8. For the as-received sample, except for several peel offs at the periphery of the worn surface, the whole fretting area is covered by hard oxide shell induced by oxide wear (see Fig. 8(a1) and (a2)). After the FsLSP treatment, the total area suffered from oxide wear is reduced markedly. For the sample treated with 50 μJ,

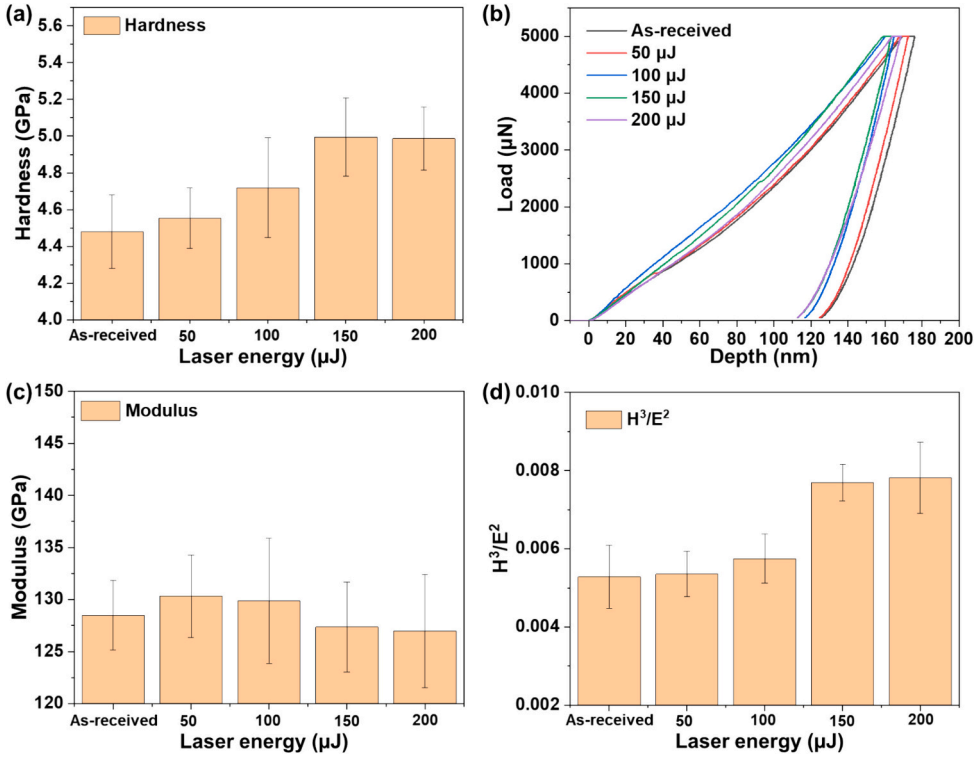

Fig. 5. (a) Surface hardness, (b) corresponding loading and unloading curves, (c) Modulus and (d) H^3/E^2 ratio of the as-received and FsLSP treated samples.

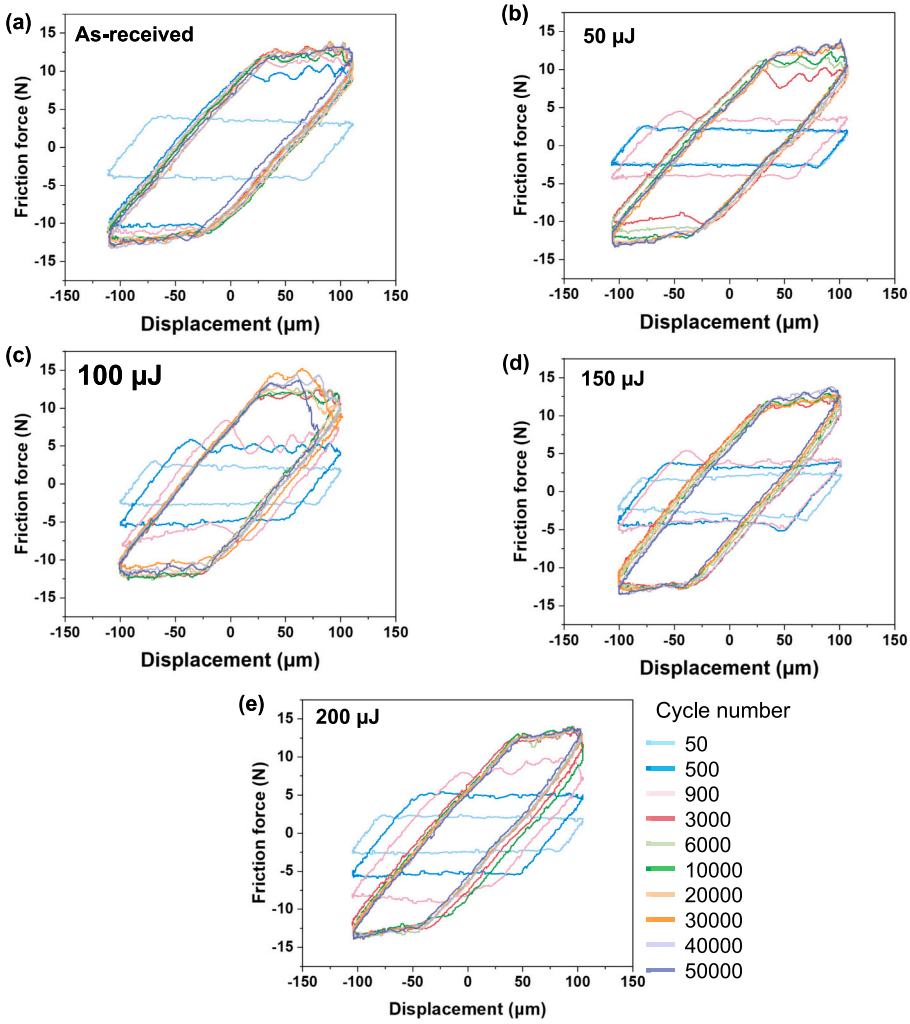

Fig. 6. (a-e) Hysteresis loops of various samples at different fretting cycles. (a) indicates the as-received sample, while (b-e) denote the samples treated with 50, 100, 150, 200 μJ femtosecond laser, respectively.

the oxide wear is almost occurred on the most fretting surface, while a large area of oxide shell is located at the center of the fretting area and the area of peel offs is reduced (see Fig. 8(b1) and (b2)). As the laser energy increases, the area suffering from oxide wear decreases and peel offs appear at the center of the worn morphology.

Worn morphologies of various samples at higher magnification are shown in Fig. 9. For the as-received sample, the whole fretting surface consists of oxide shells induced by oxide wear and pits caused by peeling off. The area between the oxide shells enclosed in the rectangular box labelled 'b' in Fig. 9(a) is shown in Fig. 9(b). It indicates that the oxide shell is easy to break and thus induces micro cracks near it. Moreover, the edges of the pits, enclosed in the rectangular box labelled 'd' in Fig. 9 (c), exhibit the plastic deformation traces perpendicular to the fretting direction (see Fig. 9(d)), indicating the poor wear resistance of the as-received Ti64. Different from the as-received sample, the pits in the sample treated with 100 and 200 μJ show no plastic deformation traces but considerable wear debris (see Fig. 9(f) and (h)), which is attributed to the increased H^3/E^2 ratio after the FsLSP treatment. Specifically, the sample treated with 200 μJ exhibits the highest H^3/E^2 ratio (see Fig. 5 (d)), which indicates that it undergoes minimal plastic deformation. Due to the dramatically decreased plasticity of the surface layer, excessive strain accumulates within the hardened layer. Consequently, the layer delaminates at the edges of pits in the sample treated with 200 μJ. Therefore, it is concluded that with increasing laser energy, the FsLSP treated surfaces are unable to accommodate plastic deformation and become more susceptible to delamination, which facilitates enhanced debris formation, which in turn, leads to more intense abrasive wear.

The wear scar profiles of all samples perpendicular to the fretting direction are shown in Fig. 10(a). The maximum wear depth in the as-received and FsLSP treated samples, with the exception of the 200 μJ sample, are ~10 μm. In the as-received sample, the wear scar is relatively shallow and flat in the center, which suggests the occurrence of severe abrasive wear in the peripheral area. Similar wear scar profiles on titanium alloys have been reported previously [43]. In contrast, the wear scar profiles of samples treated with 50, 100, and 150 μJ laser energies have a wave-like shape, which suggests that they undergo relatively uniform fretting wear. Finally, in the 200 μJ sample, the wear scar has a maximum depth of 14 μm and a V-shaped profile, which is indicative of pronounced abrasive wear on the whole fretting surface. The wear volumes and wear rates of different samples are shown in Fig. 10(b). Note that the wear volume of the as-received sample is $13.8 \pm 1.0 \times 10^5$ μm^3, whereas that of the 50 μJ sample is lesser. On samples that are treated with higher laser energies, the wear volume first decreases and then dramatically increases. In fact, the wear volume of the 100 μJ sample is only approximately $11.9 \pm 0.1 \times 10^5$ μm^3, which is around 80 % and 70 % of that of the 150 and 200 μJ samples. The variations in wear rate and wear volume with increasing laser energy have identical trends. Therefore, the FsLSP treatment with 100 μJ laser of Ti64 limits the depth of the wear scar and also reduces the overall wear volume and wear rate.

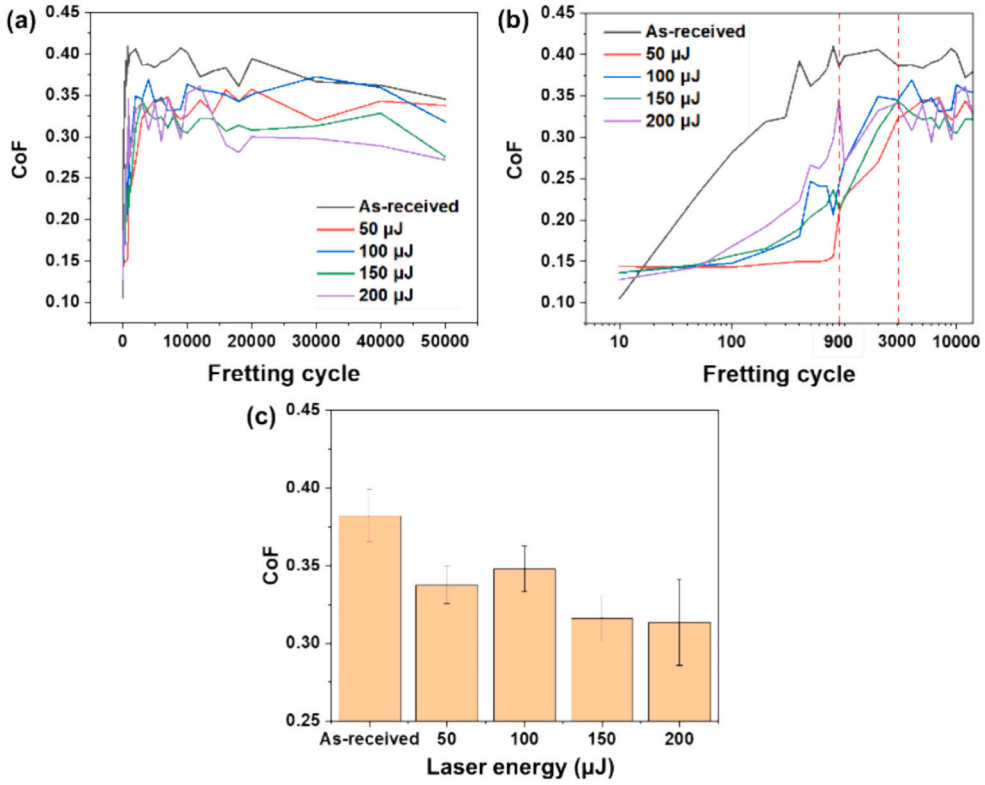

Fig. 7. Variations of CoF as a function of fretting cycles for (a) the whole 50,000 cycles and (b) the first 10,000 cycles for all the samples. (c) Average CoF of the samples in the dynamic equilibrium stage.

Overall, there are three stages of wear, characterized by distinct changes in the frictional force and CoF. In all the three stages, CoF of the as-received sample is the highest, whereas that of the FsLSP treated samples is lower. Of the FsLSP treated samples, the rate of increase in CoF increases with increasing laser energy employed for performing FsLSP. Fretting damage occurs via a mixture of oxide and abrasive wear mechanisms that are active in the as-received sample. However, with increasing laser energy employed for FsLSP, the abrasive wear mechanism becomes dominant. Finally, the wear volume after the end of the test is lowest for the 100 μJ sample followed by the 50 μJ sample. However, samples treated with higher laser energy, have higher wear volume.

3.4. Microstructural evolution and hardness of the FsLSP treated sample

Considering that the 100 μJ sample exhibits the best fretting wear resistance amongst others, its sub-surface microstructure and hardness are further investigated. Fig. 11 shows H variations of the sample as a function of the distance from the surface of the sample, d_s. As mentioned earlier (see Fig. 5), H near the surface is 4.7 ± 0.3 GPa. As d_s increases from 5 to 35 μm, H first increases with increasing d_s, i.e. it is 5.8 ± 0.3 GPa at d_s ~15 μm, and then decreases to 4.6 ± 0.2 GPa at d_s ~35 μm. In contrast, as d_s increases from ~35 to 100 μm, H monotonically increases with increasing depth and is 5.2 ± 0.3 GPa at a depth of 100 μm. Finally at d_s ~120 μm, H drops to 4.5 ± 0.2 GPa and remains almost invariant with further increase in d_s. Since H of as-received Ti64 is 4.5 ± 0.2 GPa (see Fig. 5), an approximate estimate of the laser affected depth in the 100 μJ sample is ~120 μm. Moreover, on the basis of H variations at different intervals of d_s, the laser affected layer can be further divided into two zones. The region that extends from the surface to d_s ~35 μm, since the hardness is 29 % higher than that of the matrix, is expected to have undergone intense plastic deformation. Therefore, this is referred to as a severe plastic deformation (SPD) zone. The region extending from d_s ~ 35 μm to 100 μm has intermediate H and, hence, is referred to as the mild plastic deformation (MPD) zone. Note that the depth of the laser affected zone in conventional nanosecond laser shock peening is >1 mm, which is much higher than that occurs in FsLSP processing [18,44]. This is attributed to the shorter pulse duration of the laser, that results in a smaller duration for the laser-induced shockwave to interact with the metal, which in turn reduces the depth of the laser-affected region.

The inverse pole figure (IPF-X) map of the x-z plane of the 100 μJ treated specimen is shown in Fig. 12(a). For the SPD zone, which is exposed to FsLSP, the average grain size is 2.26 ± 1.71 μm, which is 7 % finer than that in the bulk (see Fig. 2). Kernel average misorientation (KAM) maps, which provide the average misorientation angle between the crystallographic orientation of each pixel and those of its eight nearest neighbors [45,46], shown in Fig. 12(b), is a qualitative measure of the local defect mediated plastic deformation in alloys. The KAM is highest at the top of the FsLSPed surface and decreases with increasing distance from it, which implies that the extent of strain hardening also decreases from the surface to the interior of the sample.

Fig. 13 shows the grain boundary misorientation angle distributions in the SPD, MPD and matrix zones. In the grain boundary misorientation angle distribution of the SPD zone, distinct peaks are observed at 2.5°, 73.5°, 89.5°, and 93.5°. These peaks are significantly weaker in the matrix and MPD zones. These specific misorientation angles are linked to the crystallographic rotation of adjacent grains, with the Taylor axes of misorientation serving as indicators of active slip systems [47,48]. Table 2 lists the Taylor axes for various slip systems in α-Ti. Fig. 14(a) to (c) show the misorientation-axis maps in the range of ~2–5° range in different zones. In the matrix and MPD zones, the highest misorientation axis density is ~5.6 and 5.7 near the {**0 0 0 1**} plane normal. Alternately, in the SPD zone, while the axis density near the {**0 0 0 1**} plane normal decreases to 3.3, the axis density near the {**1 $\bar{1}$ 0 0**} plane normal is 1.2. In comparison, the axis density near the {**1 $\bar{1}$ 0 0**} plane normal in the MPD and matrix zones are only 0.9 and 0.8, respectively. This suggests that both basal <a> and prismatic <a> slip systems are active in

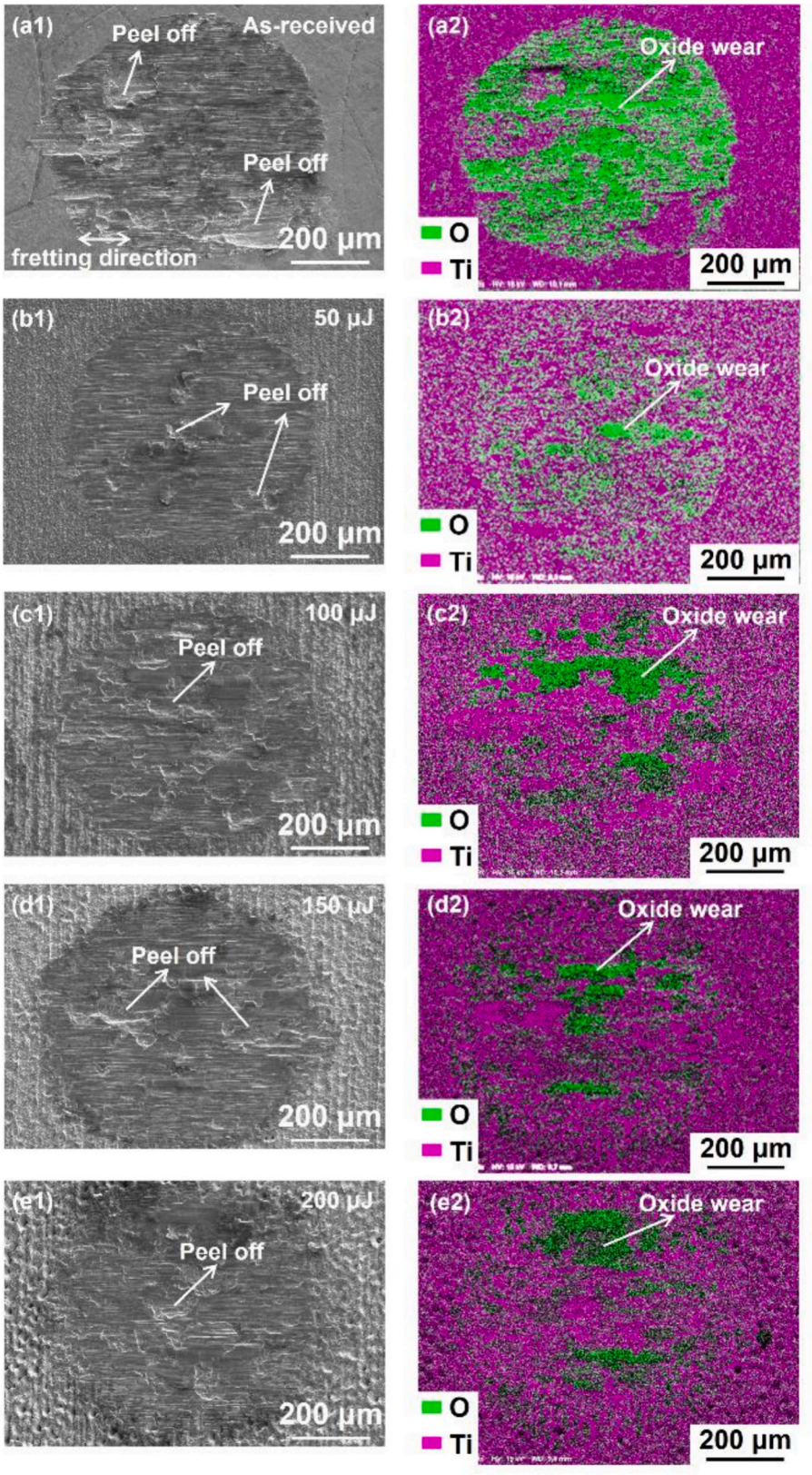

Fig. 8. (a1-e1) worn morphologies of various samples and (a2-e2) corresponding EDS mapping superimposed with the elements of oxygen and titanium. (a) indicates the as-received sample, while (b-e) denote the samples treated with 50, 100, 150, 200 μJ femtosecond laser, respectively.

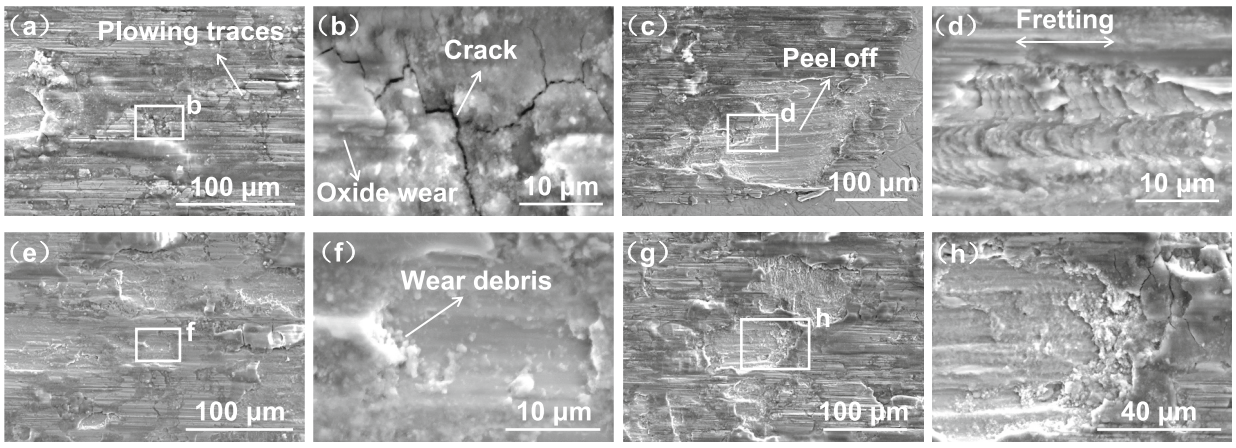

Fig. 9. Worn morphologies of various samples at high magnification. (a-d) are denoted as the as-received sample, while (e-f) and (g-h) are the sample treated with 100 and 200 μJ, respectively.

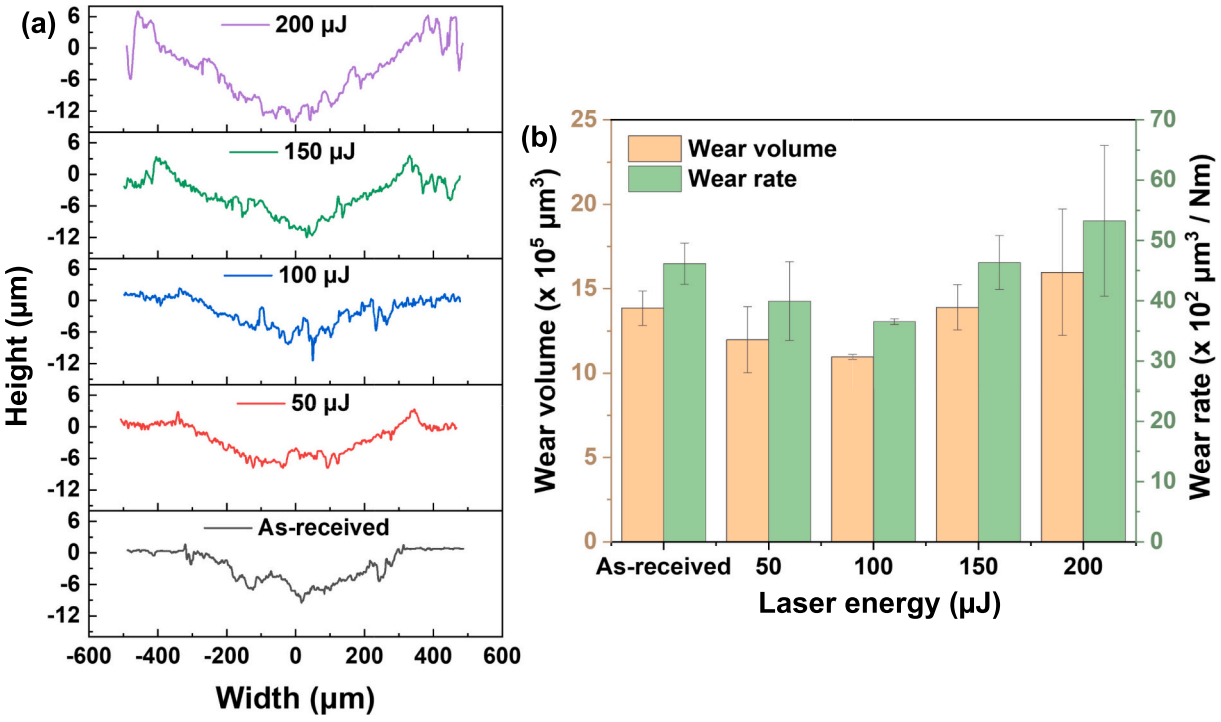

Fig. 10. (a) Wear scar profiles and (b) wear volume, wear rates of various samples after 50,000 fretting cycles.

the SPD zone whereas only prismatic <a > slip is active in the matrix and MPD zone.

Misorientation-axis maps in the range of 70–75°, 81–91° and 91–94° in the SPD zone are shown in Fig. 14(d), (e) and (f). The axis density is maximum at 73.5° near the $\{\bar{1}\,2\,\bar{1}\,0\}$ plane normal and also at 93.5° near the $(\bar{9}\,12\,\bar{3}\,5)$ plane normal. Additionally, in the misorientation-axis map for the SPD zone at the angle of 89.5° (see Fig. 14(e)), the prominent peaks cluster around the $\{1\,\bar{1}\,0\,0\}$ and $\{\bar{1}\,2\,\bar{1}\,0\}$ plane normals. Analysis of this map, in conjunction with the misorientation angle/axis pairs of twin systems in α-Ti, listed in Table 3 [49], indicates that the $\{1\,0\,\bar{1}\,2\}$ and $\{1\,1\,\bar{2}\,3\}$ twin systems are activated within the SPD zone. Note that the *c*-axes of most α-Ti grains are parallel to the *y*-direction in the as-received sample (see Fig. 2) and the laser shock wave applies compression along the *z*-direction. In this orientation, Ti64 is predisposed to nucleate $\{1\,0\,\bar{1}\,2\}$ and $\{1\,1\,\bar{2}\,3\}$ tension twins [50].

Next, *H* variations of the 200 μJ sample as a function of d_s is shown in Fig. 15. *H* is ~5.6 ± 0.7 GPa close to the surface but decreases to 5.1 ± 0.6 GPa with increasing d_s (~20 μm). Thereafter, up to d_s ~160 μm, *H* remains broadly constant, barring some minor fluctuations. In regions where d_s > 160 μm, *H* decreases further, which indicates that the laser affected layer depth of the 200 μJ sample is ~160 μm. Note that the laser affected depth of 200 μJ sample is 40 μm higher than that of 100 μJ sample. From the hardness measurements, the laser effected zone is further divided into SPD zone (0–20 μm), MPD zone (20–160 μm) and unaffected matrix (160–200 μm).

Comparing the IPF and KAM maps of the 200 μJ sample to the 100 μJ one (Fig. 16), is it evident that the surface roughness, KAM (up to 3°), and the extent of plastic deformation is higher in the former.

Fig. 17 shows the Grain boundary misorientation angle distribution in the α phase at different zones. Similar to that observed in the 100 μJ sample, the grain boundary misorientation angle distribution of the SPD zone in 200 μJ sample shows distinct peaks at 2.5°, 73.5°, 89.5°, and 93.5°. To ascertain the dominant slip systems in 200 μJ sample, the

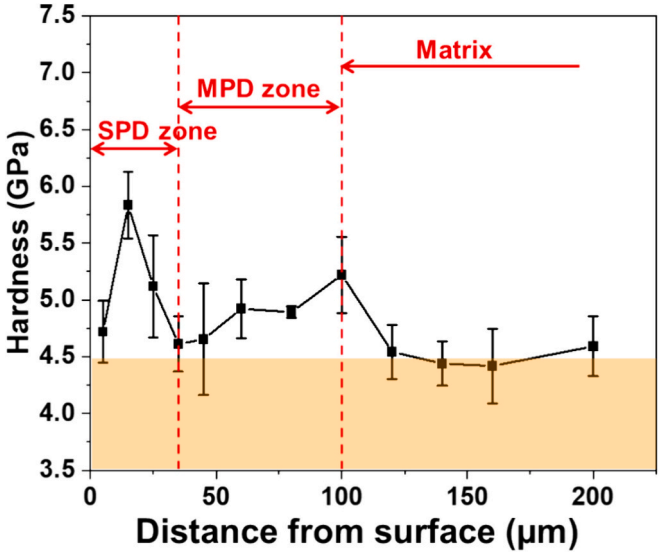

Fig. 11. Variations of hardness as a function of distance from the surface of the 100 μJ sample.

misorientation-axis maps in the range of ~2–5° range in different zones are shown in Fig. 18(a) to (c). Both prismatic <a> and basal <a> slip systems are activated in the SPD zone and the prismatic <a> slip system become dominant as the depth increases. Local maxima are also observed near the 75°/{$\bar{1}$ 2 $\bar{1}$ 0} and 93.5°/{$\bar{\mathbf{9}}$ **12** $\bar{\mathbf{3}}$ **5**} poles (Fig. 18 (d) and (f)). Moreover, the prominent peaks around the {**1** $\bar{\mathbf{1}}$ **0 0**} and {$\bar{\mathbf{1}}$ **2** $\bar{\mathbf{1}}$ **0**} plane normals indicate that the {**1 0** $\bar{\mathbf{1}}$ **2**} and {**1 1** $\bar{\mathbf{2}}$ **3**} twin systems are activated in the SPD zone (see Fig. 18(e)). Overall, the microstructural evolution of the 200 μJ sample is similar to that observed in the 100 μJ sample.

To obtain more high-resolution microstructural details of the top surface in the FsLSP treated sample, TEM analysis is performed on the 100 μJ sample. In the TEM image of the top surface, shown in Fig. 19(a), the top-most layer, which has a bright contrast, is the protective carbon film that is deposited on the surface before the TEM specimen lift-out process. A portion of the top surface, which is enclosed within the rectangular box labelled 'b' in Fig. 19(a), is magnified, and shown in Fig. 19(b). As was observed earlier in the SEM images (see Fig. 4(a)), the top surface, which is below the protective carbon film, of the FsLSP treated Ti64 is undulated. Moreover, there are several regions within the top surface, which have a brighter contrast. To analyze the composition in this layer, energy dispersive X-ray spectroscopy (EDX) was performed, and the corresponding Ti, C and O maps are shown in Fig. 19(c)-(e). It was determined that the top layer (below the carbon film), whose thickness varies from 540 to 1000 nm, is uneven and rich in oxygen, which implies that it has transformed to a metal oxide. Since the regions with brighter contrast do not contain Ti or O (see Fig. 19(b)), they are likely to be pores or voids. These pores have sizes that range from 40 to 250 nm and are mostly concentrated at the interface between the metal oxide layer and the unoxidized metal substrate. Previous studies on ultra-short duration laser treatment of metals have suggested that the formation of such nanocavities below the surface [51–53] are an outcome of implosion of bubble clusters that form during ablation. Also, the HRTEM image obtained from the region enclosed in the rectangular box labelled 'f' in Fig. 19(a), shown in Fig. 19(f), reveals that a few tens of nm thick nanocrystalline layer exists at the interface of the metal-oxide interface.

4. Discussion

4.1. Deformation mechanisms in Ti64 during FsLSP treatment

In the FsLSP treatment, laser induced shock waves create a rapid increase in pressure to ~10^2–10^3 GPa over a sample within a few picoseconds, which then decays over tens of picoseconds [54]. Within this duration, the surface layer of the sample deforms at a strain rate of ~10^9 s^{-1} [55–57], and the peak pressure generated by the laser induced shock wave causes strain hardening [58]. Since the intensity of the laser shock wave pressure is proportional to the laser energy, FsLSP performed with higher laser energy leads to enhancement in surface hardening, which was indeed observed in this study (see Fig. 5). And the increased laser shock wave pressure is beneficial to increase the laser effective depth (see Fig. 11 and Fig. 15). However, beyond a certain energy threshold, the laser ionizes the surrounding air medium, which leads to the formation of plasma. The subsequent absorption and scattering of laser energy by plasma due to dielectric breakdown reduces the amount of laser energy reaching the surface, which in turn diminishes the laser shock wave pressure. Moreover, increased laser energy intensifies ablation, which generates heat on the surface layer. This heat can anneal and relax the shock wave induced compressive residual stresses on the surface. The invariance in hardness when laser energy >150 μJ (see Fig. 5) is attributed to these effects.

Laser shock wave induced strain hardening and plastic deformation in Ti64, which is mediated by dislocations and twins, also leads to a significant change in the microstructure, as is seen in the SPD zone (see Fig. 13, Fig. 17 and Table 2). Previous studies have indicated that the high misorientation density along 30°/{**0 0 0 1**}, 75°/{$\bar{1}$ 2 $\bar{1}$ 0}, and 93.5°/{$\bar{\mathbf{9}}$ **12** $\bar{\mathbf{3}}$ **5**} axes [18,59] are an indication of recrystallization in α-Ti. However, this dynamic recrystallization is not likely to be driven by laser heating as the radial extent of the heat-affected zone in the FsLSP treatment is <2 μm [60], whereas dynamic recrystallization is observed up to a depth of 35 μm in the SPD zone of 100 μJ sample. We believe that the observed dynamic recrystallization is attributed to the high strain rate deformation induced temperature rise (ΔT) during FsLSP. ΔT due to high-strain-rate deformation can be estimated using the equation [61],

$$\Delta T \approx \frac{\beta}{\rho C_V} \cdot P \cdot \varepsilon, \tag{1}$$

where $\boldsymbol{\beta}$ is the heat-work conversion coefficient, which is ~0.9, $\boldsymbol{\rho}$ ~4.43 g/cm^3 is the density of Ti64, $\boldsymbol{C_V}$ ~0.5263 J • $\boldsymbol{g^{-1}}$ • $\boldsymbol{C^{-1}}$ is the specific heat capacity, $\boldsymbol{P}$ ~10^2 GPa is the pressure of the laser shock wave, and $\boldsymbol{\varepsilon}$ is the strain induced by FsLSP. $\boldsymbol{\varepsilon}$ is calculated from [61],

$$\boldsymbol{\varepsilon} = \dot{\boldsymbol{\varepsilon}} \times \mathbf{t}, \tag{2}$$

where $\dot{\boldsymbol{\varepsilon}}$ ~10^9 s^{-1} is the strain rate of FsLSP, and $\boldsymbol{t}$ is the duration time of femto-second laser shock wave. For FsLSP treated with 100 μJ, the pulse width of the shock wave is approximately a hundred times that of the laser pulse width [62], which translates to a shock wave duration of **100** × **290** fs = 29 ps. Using Eq. (2), the calculated $\boldsymbol{\varepsilon}$ during FsLSP is ~0.029. Substituting these in Eq. (1), the calculated ΔT is ~1119 °C. Considering that the FsLSP treatment was performed in ambient conditions, the peak temperature within the surface during FsLSP is 1144 °C, which is considerably higher than the recrystallization temperature of Ti64, which is ~664 °C [63,64]. This implies that the dynamic recrystallization observed in the SPD zone is a consequence of the shock wave generated by the femtosecond laser.

Since the SPD zone is in the closest proximity to the surface, the material within it undergoes more intense plastic deformation than that in the MPD zone. Prismatic <a> slip is easily activated due to its lowest critical resolved shear stress (CRSS) [65–67], and the basal <a> slip systems, with the second lowest CRSS, are also activated owing to the considerably high stresses and strains that develop during FsLSP.

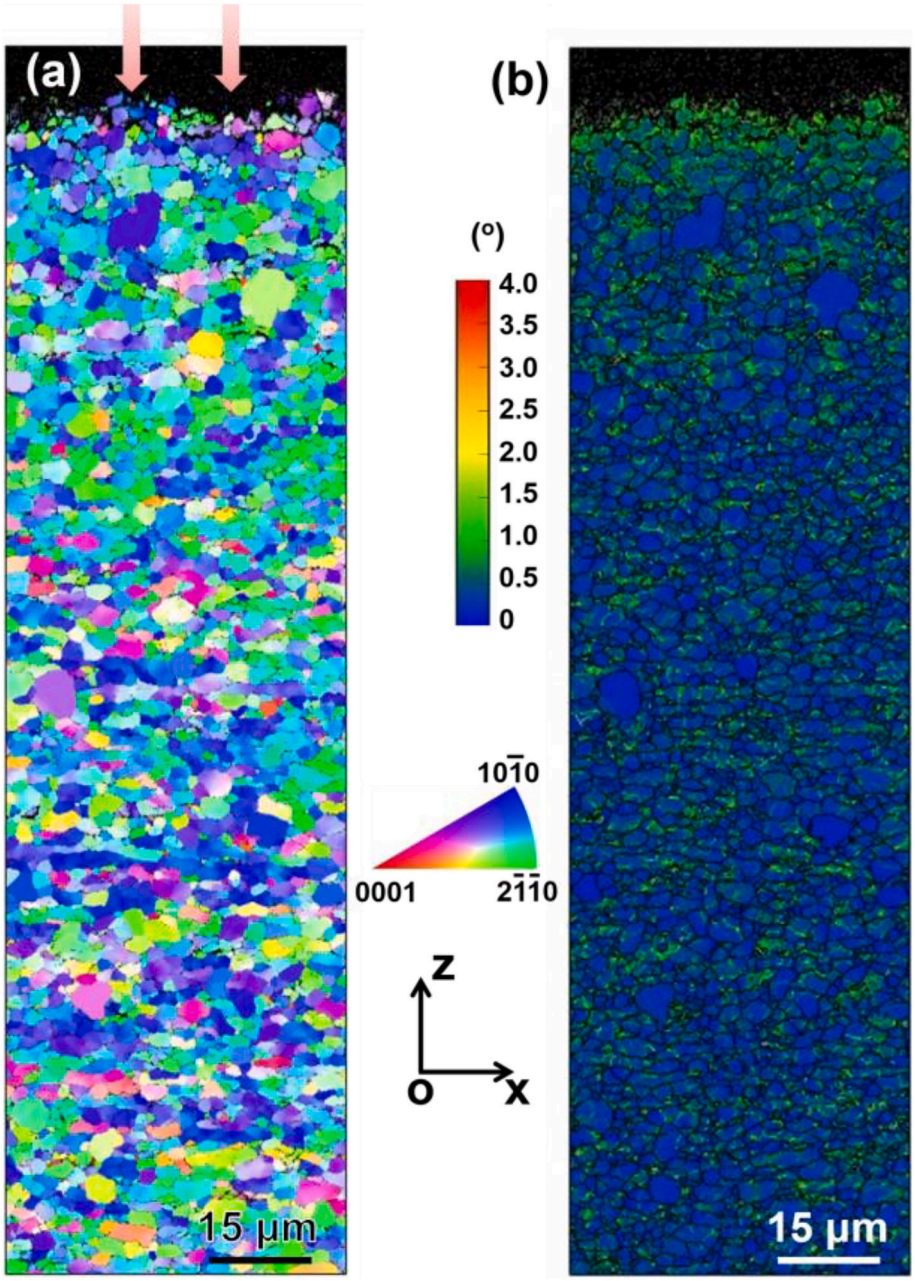

Fig. 12. EBSD maps of the cross-sectional *xz*-plane near the shocked surface of 100 μJ sample. (a) Inverse pole figure map along the *x*-axis, with the peak arrows denoting the laser irradiation direction; (b) KAM map.

However, note that these systems account for only four independent slip systems, whereas the von Mises criterion asserts that for homogeneous plastic deformation, at least five independent slip systems must be activated [67]. We believe that the requirement of an additional avenue for deformation is fulfilled by the formation of tension $\{\mathbf{1\,0\,\bar{1}\,2}\}$ and $\{\mathbf{1\,1\,\bar{2}\,3}\}$ twins (see Fig. 14(e), Fig. 18 (e) and Table 3). The rationale behind the formation of twins is as follows. Note that the shock wave induced strain rate is highest at the top surface of the alloy but diminishes rapidly with the increasing distance from it [68]. Therefore, the strain rate is highest in the SPD zone but lower in the MPD zone and lowest in the underlying matrix. Considering that the CRSS for Prismatic <a> slip increases with increasing strain rate [69], there is a high likelihood that other slip and twin systems may instead occur in the SPD zone. To accommodate the plastic deformation, basal <a> slip and $\{1\,0\,\bar{1}\,2\}$ and $\{1\,1\,\bar{2}\,3\}$ tension twins are generated within the SPD zone. Also, note that, in the SPD zone, the occurrence of laser shock wave induced recrystallization also leads to grain refinement. In fact, besides strain hardening, the Hall-Petch strengthening from this grain refinement is an additional contribution to the hardness of the SPD zone (see Fig. 11). In contrast, in the MPD zone, plastic deformation is mitigated as the intensity of the laser shock wave diminishes with depth. Since this zone is not deformed severely as that of SPD zone at an ultra-high strain rate, prismatic <a> slip becomes the dominant mode of plastic deformation. This leads to moderate strain hardening, which, in turn, manifests as a slight increase in the hardness of the MPD zone compared to that of the underlying matrix (see Fig. 11).

4.2. *Fretting wear mechanism*

The variations in CoF in the initial, escalation, and dynamic equilibrium stages of fretting wear dictate the overall wear behavior of the as

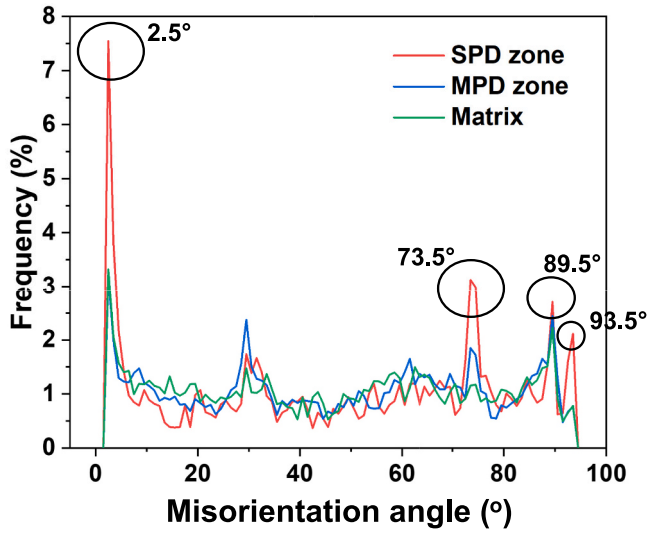

Fig. 13. Grain boundary misorientation angle distribution of α phase at different zones in the 100 μJ sample.

Table 2
The slip systems in α Ti and corresponding Taylor axes [47,48].

Slip systems		Taylor axis
Basal <a>	$\{0\,0\,0\,1\}\langle 1\,1\,\bar{2}\,0\rangle$	$\langle 1\,0\,\bar{1}\,0\rangle$
Prismatic <a>	$\{1\,0\,\bar{1}\,0\}\langle 1\,1\,\bar{2}\,0\rangle$	$\langle 0\,0\,0\,1\rangle$
Pyramid <a>	$\{1\,0\,\bar{1}\,1\}\langle 1\,1\,\bar{2}\,0\rangle$	$\langle \bar{1}\,0\,1\,2\rangle$
Pyramid (1st) < a + c>	$\{1\,0\,\bar{1}\,1\}\langle 1\,1\,\bar{2}\,3\rangle$	$\langle \bar{1}\bar{3}\,8\,5\,3\rangle$
Pyramid (2st) < a + c>	$\{1\,1\,\bar{2}\,1\}\langle 1\,1\,\bar{2}\,3\rangle$	$\langle 6\,\bar{1}\,\bar{5}\,3\rangle$
Pyramid (3st) < a + c>	$\{1\,1\,\bar{2}\,2\}\langle 1\,1\,\bar{2}\,3\rangle$	$\langle \bar{1}\,0\,1\,0\rangle$

received and FsLSP treated samples. In the initial stage, the surface roughness, and hence the effective contact area between the Si_3N_4 ball and the sample surface, determines CoF. Since the as-received sample is flat whereas that of the FsLSP treated samples contain undulations or asperities on the surface, the contact area of the latter with the Si_3N_4 ball is lesser than that of the former. In fretting, a higher contact area leads to greater surface adhesion and an increase in CoF [12,70]. This explains the low CoF and frictional force in the FsLSP treated samples compared to that of the as-received sample in the initial stage of fretting (see Fig. 6). As suggested by Zhou and Vincent [71,72], a change in the shape of the parallelogram-shaped hysteresis loop (see Fig. 6) is indicative of deformation occurring in the gross slip regime, where the top surface of the sample gets worn out. The reason this transition occurs at 50 cycles in the as-received sample, but much later in the FsLSP treated samples (see Fig. 6), is that the latter is covered with metal oxide asperities (see Fig. 8). However, since the tips of asperities contain several nanocavities (see Fig. 19), it is vulnerable to undergo degradation over time. Therefore, in the escalation stage, asperities on the FsLSP treated samples begin to break extensively due to the ongoing fretting wear. Such disintegration of asperities leads to direct contact between the Si_3N_4 ball and sample surface, resulting in surface scratches and thus an increase in CoF of the FsLSP treated samples (see Fig. 7(b)). Since the size of asperities are larger in the 150 and 200 μJ samples, only parts of asperities are destroyed during the dynamic equilibrium stage of wear. Due to the relatively decreased contact area with the Si_3N_4 ball and the existence of wear debris layer [42,73], the samples treated with higher laser energies exhibit lower CoF. Though the asperities of the 50 and 100 μJ samples are nearly wiped out during the dynamic equilibrium stage, CoF of them is still lesser than the as-received sample because of the surface strain hardened layer [11,74].

According to the Archard's law [75], the wear rate is inversely proportional to the hardness. Since the hardness of the 100 μJ sample is higher than that of the as received and 50 μJ sample, it has a lower wear volume and wear rate (see Fig. 10(b)). However, the wear rates of the 150 and 200 μJ samples which have higher hardness than the 100 μJ sample, do not appear to follow the above-expected correlation. Note that Archard law is formulated on the basis of the flattened asperity model [75], which implies that for the FsLSP treated, rough surface, the total wear volume is the summation of the material wear at all asperities.

Table 3
The misorientation angle/axis pairs of the tension and compression twin systems in Ti [49].

Twin mode	System	Misorientation angle/axis
Tension twin 1	$\{1\,0\,\bar{1}\,2\}\langle \bar{1}\,0\,1\,1\rangle$	85.49° along $\langle 1\,1\,\bar{2}\,0\rangle$
Tension twin 2	$\{1\,1\,\bar{2}\,1\}\langle \bar{1}\,\bar{1}\,2\,6\rangle$	34.69° along $\langle \bar{1}\,0\,1\,0\rangle$
Tension twin 3	$\{1\,1\,\bar{2}\,3\}\langle \bar{1}\,\bar{1}\,2\,2\rangle$	86.27 ° along $\langle \bar{1}\,0\,1\,0\rangle$
Compression twin 1	$\{1\,1\,\bar{2}\,2\}\langle 1\,1\,\bar{2}\,\bar{3}\rangle$	63.98° along $\langle \bar{1}\,0\,1\,0\rangle$
Compression twin 2	$\{1\,0\,\bar{1}\,1\}\langle \bar{1}\,0\,1\,2\rangle$	56.82° along $\langle 1\,1\,\bar{2}\,0\rangle$
Compression twin 3	$\{1\,1\,\bar{2}\,4\}\langle 2\,2\,\bar{4}\,\bar{3}\rangle$	77.35° along $\langle \bar{1}\,0\,1\,0\rangle$

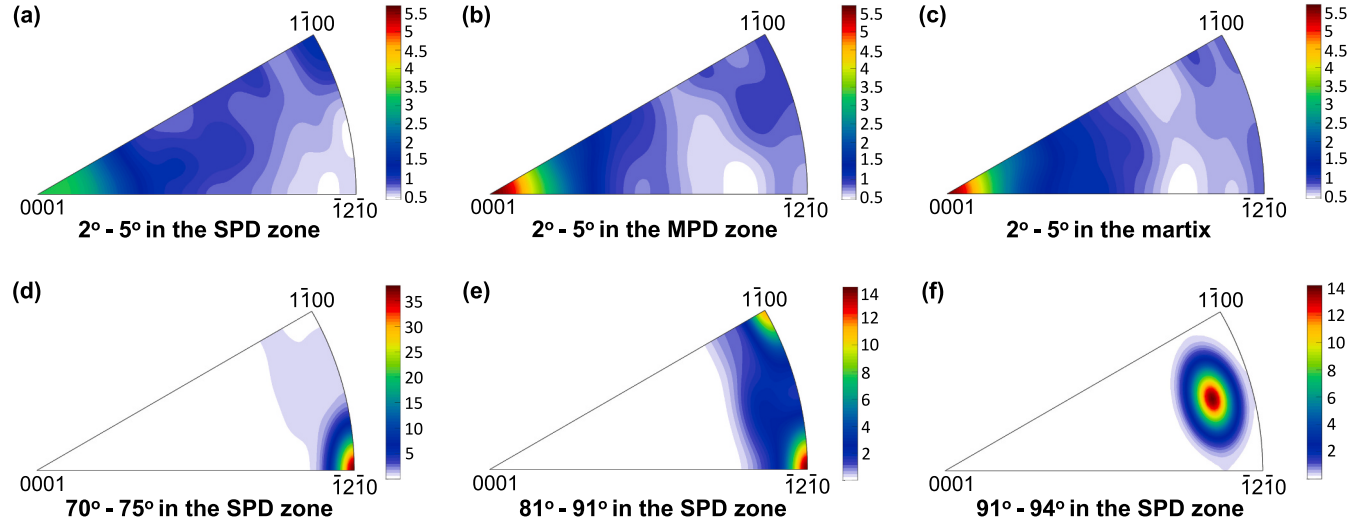

Fig. 14. Misorientation-axis maps of α phase in the 100 μJ sample: (a) 2–5° in the SPD zone; (b) 2–5° in the MPD zone; (c) 2–5° in the matrix; (d) 70–75° in the SPD zone; (e) 87–91° in the SPD zone; (f) 91–94° in the SPD zone.

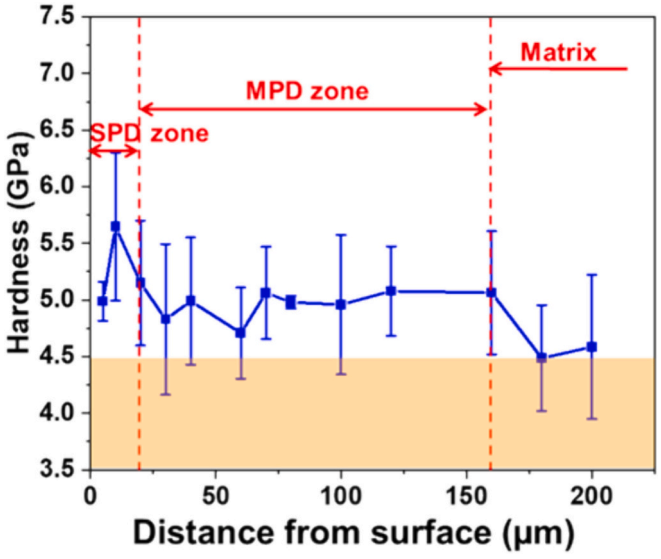

Fig. 15. Variations of hardness as a function of distance from the surface of the 200 μJ sample.

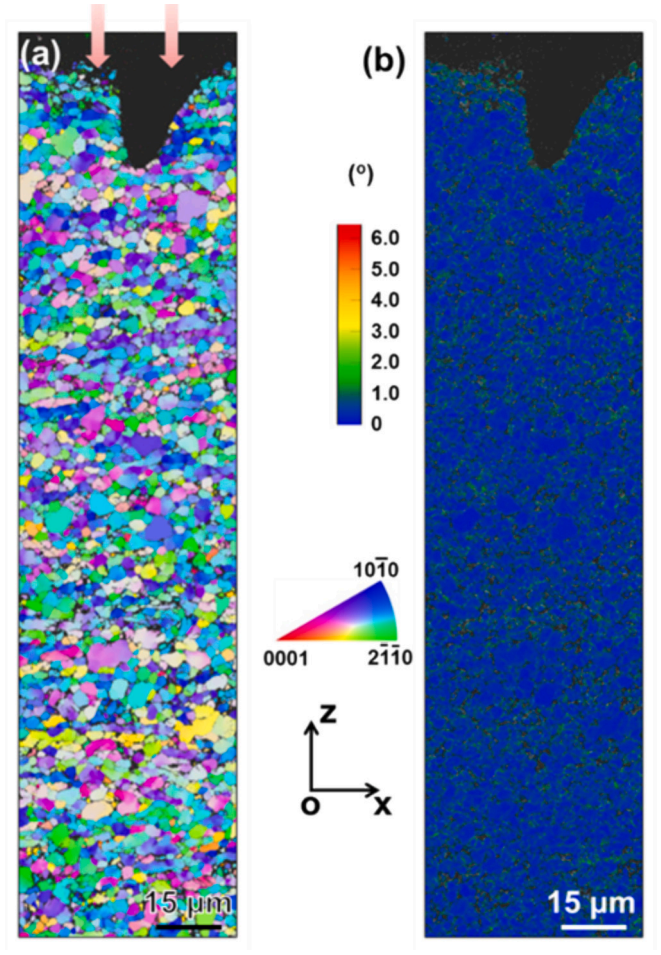

Fig. 16. EBSD maps of the cross-sectional xz-plane near the shocked surface of 200 μJ sample. (a) Inverse pole figure map along the x-axis, with the peak arrows denoting the laser irradiation direction; (b) KAM map.

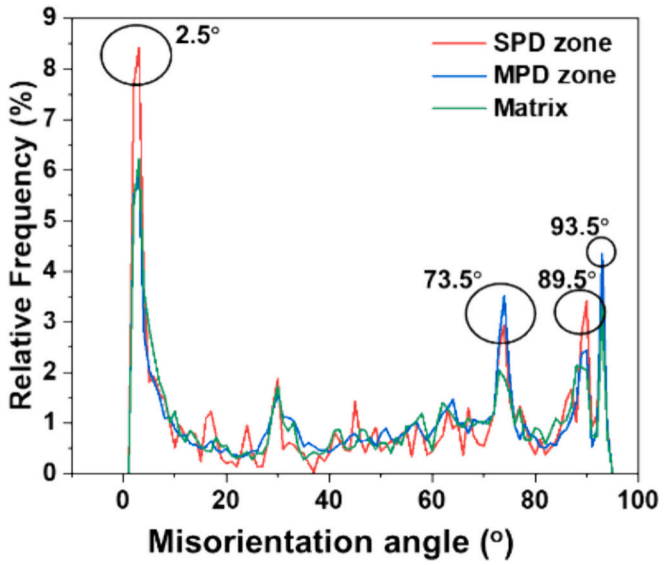

Fig. 17. Grain boundary misorientation angle distribution of α phase at different zones in the 200 μJ sample.

While the surface asperities on the 150 and 200 μJ samples are more prominent than that on the 100 μJ sample, they are more fragile owing to the formation of larger laser ablation induced voids [76]. Therefore, during the wear of the 150 and 200 μJ samples, comparatively more debris is produced, which acts as abrasive media. We believe that the increased wear rate in the 150 and 200 μJ samples are an outcome of the formation of excessive debris, which enhances abrasive wear of their surfaces.

Based on the above analysis, the schematic diagram of fretting wear mechanism of various specimens is shown in Fig. 20. In the as-received sample, the top surface is contact with Si_3N_4 ball directly at the initiation of the fretting wear (see Fig. 20(a)). Due to its low hardness, the fretting surface of the as-received sample gets worn fast and produces wear debris. Under the influence of frictional heat produced by fretting wear, these wear debris form the oxide shell covered on the fretting surface. However, the oxide shell is so brittle that it is easy to break. Once the outer oxide shell gets destroyed, the inner Ti64 matrix is exposed. With the grinding of the hard debris, the fretting surface is worn further and plastic deformation traces perpendicular to the fretting direction occur at the pits where the Ti64 matrix is exposed. Therefore, oxide wear and abrasive wear are the dominant fretting wear mechanism in the as-received sample.

In the sample treated with a lower laser energy, the top surface is covered with asperities with a height of ~5 μm and thus results in the reduced CoF due to the decreased contact area at the initial stage of wear. However, the tip of asperities contains a few nanocavities, which make it fragile. With the progress of fretting wear, the whole asperities are wiped out and the Si_3N_4 ball comes into direct contact with the surface strain hardened layer (see Fig. 20(b)). It has been reported that a significant microstructural refinement can result in a higher resistance to its oxidation [10]. Thus, the reduced area covered by oxide shell is attributed to the grain refinement of the surface after the FsLSP treatment. The surface strain hardened layer improves its wear resistance and thus results in reduced wear volume. So, for the sample treated with lower laser energy, the oxide wear contribution decreases, making the abrasive wear the dominant fretting wear mechanism.

For the sample treated with higher laser energies, the height of asperities increases and could be up to ~22 μm. Like the sample treated with lower laser energy, the Si_3N_4 ball comes into contact with the tip of asperities initially. However, since the pores inside the asperities are larger (due to increased laser fluence [53]), the asperities are more

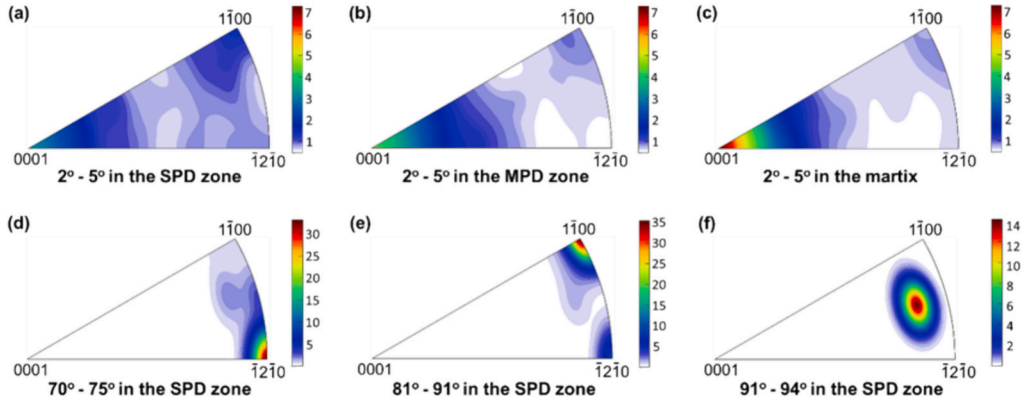

Fig. 18. Misorientation-axis maps of α phase in the 200 μJ sample: (a) 2–5° in the SPD zone; (b) 2–5° in the MPD zone; (c) 2–5° in the matrix; (d) 70–75° in the SPD zone; (e) 87–91° in the SPD zone; (f) 91–94° in the SPD zone.

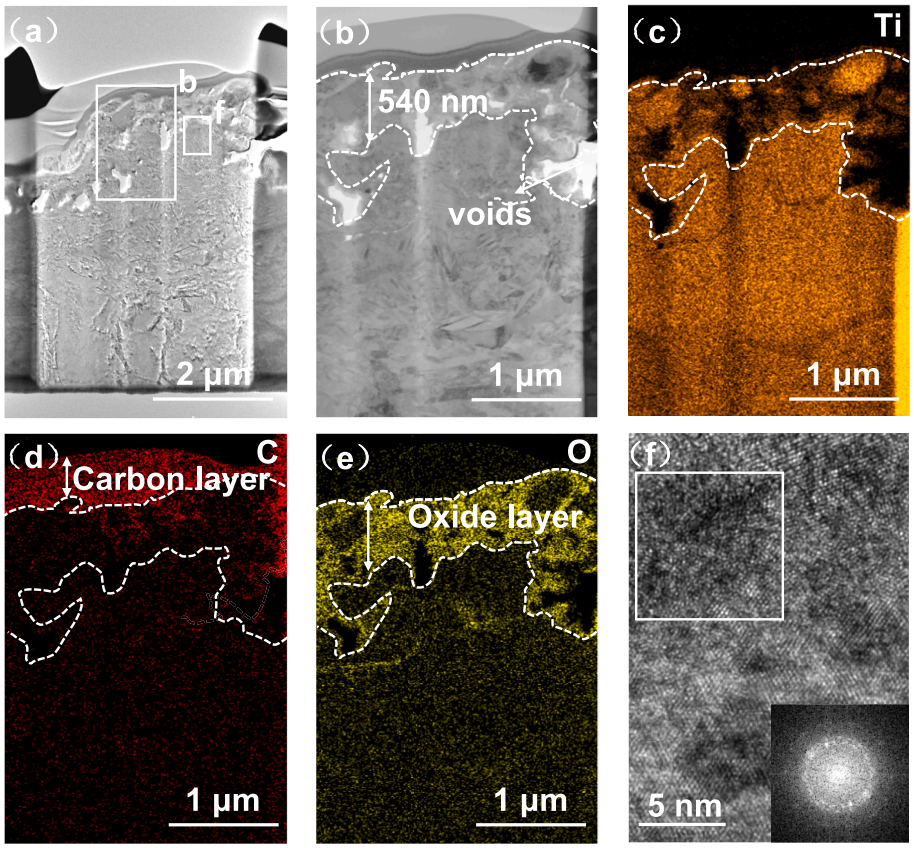

Fig. 19. TEM characterization of the 100 μJ sample surface. (a) the overall view of the top surface parallel to the *xz*-plane; (b-e) the enlarged image of area marked as b in (a) and the corresponding EDX analysis; (f) the high-resolution TEM image of the area marked as f in (a).

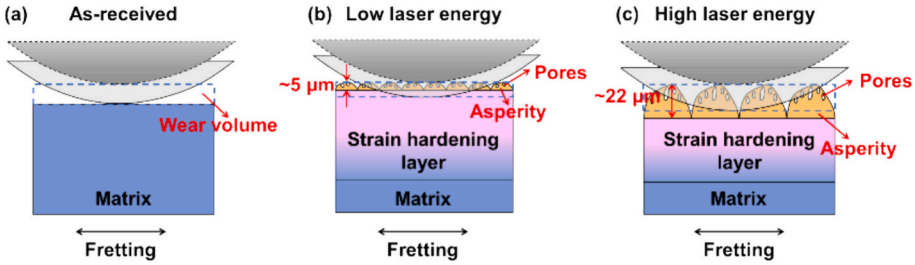

Fig. 20. Schematic diagram of the fretting wear mechanism in the as-received sample and the samples treated with lower and higher femtosecond laser energy.

susceptible to destruction. This rationalizes the increasing rate of CoF in the sample treated with 200 μJ at the initial stage of wear. With the tips of asperity worn out, the Si_3N_4 ball continues to be contact with the remains of asperities (see Fig. 20(c)). Due to the reduced contact area and wear debris interlayer, CoF in the dynamic equilibrium stage remains relatively lower. However, the hard debris from the asperities keeps grinding on the fretting surface. Besides, the surfaces treated with higher laser energies have an increased tendency for delamination owing to the significantly increased H^3/E^2 ratio. Owing to these factors, a large amount of wear volume is produced. Therefore, abrasive wear is the dominant fretting wear mechanism of the sample treated with higher laser energy.

5. Conclusion

In this study, fretting wear tests followed by microstructural, topographical and mechanical characterization are performed on as-received and FsLSP treated Ti64 alloy samples. The key conclusions of this study are as follows. An increase in the FsLSP laser energy decreases the surface coverage of LIPSSs, but increases the surface roughness and broadly the surface hardness of Ti64. Surface hardening is attributed to the severe plastic deformation initiated by the laser shock wave, which activates the prismatic <a> and basal <a> slip systems in the alloy. Furthermore, dynamic recrystallization, triggered by the temperature elevation from the ultra-high pressure of the laser shock wave, results in grain refinement within the surface layer, which supplements surface hardening via the Hall-Petch effect. A submicron-thick oxide layer and asperities form on the top layer of FsLSP treated samples, which reduces contact area and decreases the friction force and CoF during the initial stages of fretting wear. Nonetheless, these asperities, which contain nanocavities underneath, are susceptible to rapid degradation. Following degradation of the asperities, samples treated with laser energies of 50 and 100 μJ exhibit enhanced wear resistance as they have higher surface hardness. In contrast, despite having a hard surface layer, samples treated with 150 and 200 μJ undergo considerable abrasive wear, which is attributed to the generation of a higher volume of wear debris. This particular caveat suggests that the optimization of laser energy is critical in ensuring the successful implementation of FsLSP treatment for improving the fretting wear resistance of Ti64.

Novelty statement

This is the first study that systematically investigates and identifies the optimum laser power parameters that must be used in femtosecond laser shock peening (FsLSP) treatment to enhance the fretting wear resistance of Ti6Al4V alloy. The primary outcome of this study is that FsLSP treatment performed using moderate laser energies, which are of the order of 50–100 μJ, can improve the surface wear resistance whereas treatment with higher powers makes the alloy's surfaces more susceptible to fretting wear. A detailed analysis of the wear mechanisms in each condition is presented. In addition, utilizing careful EBSD analysis, a thorough explanation of the deformation mechanisms in the alloy during FsLSP is provided.

CRediT authorship contribution statement

Xuan Huang: Writing – original draft, Investigation. **Kai Chen:** Writing – review & editing, Supervision, Funding acquisition, Conceptualization. **Liucheng Zhou:** Resources, Funding acquisition. **R. Lakshmi Narayan:** Writing – review & editing, Formal analysis. **Upadrasta Ramamurty:** Writing – review & editing, Supervision.

Declaration of competing interest

The authors declare that they have no known competing financial interests or personal relationships that could have appeared to influence the work reported in this paper.

Data availability

The raw/processed data required to reproduce these findings cannot be shared at this time due to technical or time limitations.

Acknowledgements

This work is supported by the National Major Science and Technology Project of China (J2019-IV-0014-0082), National Key Research and Development Program of China (2022YFB4601700), the National Natural Science Foundation of China (W2411048, 51927801 and U2032205), and the major research plan of National Natural Science Foundation of China (9236030003). U. R. acknowledges the support from Agency for Science, Technology and Research (A*STAR) of Singapore (No. A18B1b0061). We appreciate the support from the International Joint Laboratory for Micro/Nano Manufacturing and Measurement Technologies and the Collaborative Innovation Center of High-End Manufacturing Equipment. We also thank Dr. Yuanbin Qin for TEM characterization and Instrumental Analysis Center of Xi'an Jiaotong University for the assistance with EBSD tests.

References

[1] Z.M. Wang, Y.F. Jia, X.C. Zhang, Y. Fu, C.C. Zhang, S.T. Tu, Effects of different mechanical surface enhancement techniques on surface integrity and fatigue properties of Ti-6Al-4V: a review, Crit. Rev. Solid State Mater. Sci. 44 (2019) 445–469, https://doi.org/10.1080/10408436.2018.1492368.
[2] W. Warzanskyj, I. Angulo, F. Cordovilla, M. Díaz, J.A. Porro, A. García-Beltrán, S. Cabeza, J.L. Ocana, Analysis of the thermal stability of residual stresses induced in Ti-6Al-4V by high density LSP treatments, J. Alloys Compd. 931 (2023) 167530, https://doi.org/10.1016/j.jallcom.2022.167530.
[3] C.M. Firrone, S. Zucca, Underplatform dampers for turbine blades: the effect of damper static balance on the blade dynamics, Mech. Res. Commun. 36 (2009) 515–522, https://doi.org/10.1016/j.mechrescom.2009.01.002.
[4] D. Liu, B. Tang, X. Zhu, H. Chen, J. He, J.P. Celis, Improvement of the fretting fatigue and fretting wear of Ti6Al4V by duplex surface modification, Surf. Coat. Tech. 116 (1999) 234–238, https://doi.org/10.1016/S0257-8972(99)00279-0.
[5] A. Amanov, I.S. Cho, D.E. Kim, Y.S. Pyun, Fretting wear and friction reduction of CP titanium and Ti–6Al–4V alloy by ultrasonic nanocrystalline surface modification, Surf. Coat. Tech. 207 (2012) 135–142, https://doi.org/10.1016/j.surfcoat.2012.06.046.
[6] D. Du, D. Liu, Z. Ye, X. Zhang, F. Li, Z. Zhou, L. Yu, Fretting wear and fretting fatigue behaviors of diamond-like carbon and graphite-like carbon films deposited on Ti-6Al-4V alloy, Appl. Surf. Sci. 313 (2014) 462–469, https://doi.org/10.1016/j.apsusc.2014.06.006.
[7] Q. Yang, W. Zhou, Z. Niu, X. Zheng, Q. Wang, X. Fu, G. Chen, Z. Li, Effect of different surface asperities and surface hardness induced by shot-peening on the fretting wear behavior of Ti-6Al-4V, Surf. Coat. Tech. 349 (2018) 1098–1106, https://doi.org/10.1016/j.surfcoat.2018.06.092.
[8] P.J. Golden, A. Hutson, V. Sundaram, J.H. Arps, Effect of surface treatments on fretting fatigue of Ti–6Al–4V, Int. J. Fatigue 29 (2007) 1302–1310, https://doi.org/10.1016/j.ijfatigue.2006.10.005.
[9] J.S. Hoppius, L.M. Kukreja, M. Knyazeva, F. Pöhl, F. Walther, A. Ostendorf, E. L. Gurevich, On femtosecond laser shock peening of stainless steel AISI 316, Appl. Surf. Sci. 435 (2018) 1120–1124, https://doi.org/10.1016/j.apsusc.2017.11.145.
[10] J.D. Majumdar, E.L. Gurevich, R. Kumari, A. Ostendorf, Investigation on femtosecond laser irradiation assisted shock peening of medium carbon (0.4% C) steel, Appl. Surf. Sci. 364 (2016) 133–140, https://doi.org/10.1016/j.apsusc.2015.12.058.
[11] Y. Yu, L. Zhou, Z. Cai, S. Luo, X. Pan, J. Zhou, W. He, Research on the mechanism of DD6 single crystal superalloy wear resistance improvement by femtosecond laser modification, Appl. Surf. Sci. 577 (2022) 151691, https://doi.org/10.1016/j.apsusc.2021.151691.
[12] X. Pan, W. He, Z. Cai, X. Wang, P. Liu, S. Luo, L. Zhou, Investigations on femtosecond laser-induced surface modification and periodic micropatterning with anti-friction properties on Ti6Al4V titanium alloy, Chin. J. Aeronaut. 35 (2022) 521–537, https://doi.org/10.1016/j.cja.2021.01.003.
[13] J.L. Ocaña, C. Correa, A. García-Beltrán, J.A. Porro, M. Díaz, L. Ruiz-de-Lara, D. Peral, Laser shock processing of thin Al2024-T351 plates for induction of through-thickness compressive residual stresses fields, J. Mater. Process. Technol. 223 (2015) 8–15, https://doi.org/10.1016/j.jmatprotec.2015.03.030.
[14] S.M. Yu, D.X. Liu, X.H. Zhang, C.S. Liu, A comparison study of wear and fretting fatigue behavior between Cr-alloyed layer and Cr–Ti solid-solution layer, Acta Metall. Sin.-Engl. Lett. 29 (2016) 782–792, https://doi.org/10.1007/s40195-016-0449-3.

[15] J. Tang, D. Liu, X. Zhang, D. Du, S. Yu, Effects of plasma ZrN metallurgy and shot peening duplex treatment on fretting wear and fretting fatigue behavior of Ti6Al4V alloy, Materials 9 (2016) 217, https://doi.org/10.3390/ma9040217.
[16] C. Gu, Z. Tian, J. Zhao, Y. Wang, Investigation of microstructure and tribological property of Ti-6Al-4V alloy by laser shock peening processing, Int. J. Adv. Manuf. Technol. 129 (2023) 955–967, https://doi.org/10.1007/s00170-023-12354-5.
[17] X. Yang, H. Zhang, H. Cui, C. Wen, Effect of laser shock peening on fretting fatigue life of TC11 titanium alloy, Materials 13 (2020) 4711, https://doi.org/10.3390/ma13214711.
[18] X. Huang, W. Zhu, K. Chen, R.L. Narayan, U. Ramamurty, L. Zhou, W. He, Twin and dislocation induced grain subdivision and strengthening in laser shock peened Ti, Int. J. Plast. 159 (2022) 103476, https://doi.org/10.1016/j.ijplas.2022.103476.
[19] X. Nie, W. He, L. Zhou, Q. Li, X. Wang, Experiment investigation of laser shock peening on TC6 titanium alloy to improve high cycle fatigue performance, Mater. Sci. Eng. A 594 (2014) 161–167, https://doi.org/10.1016/j.msea.2013.11.073.
[20] S. Luo, W. He, K. Chen, X. Nie, L. Zhou, Y. Li, Regain the fatigue strength of laser additive manufactured Ti alloy via laser shock peening, J. Alloy. Compd. 750 (2018) 626–635, https://doi.org/10.1016/j.jallcom.2018.04.029.
[21] H.L. Costa, J. Schille, A. Rosenkranz, Tailored surface textures to increase friction—a review, Friction 10 (2022) 1285–1304, https://doi.org/10.1007/s40544-021-0589-y.
[22] J. Bonse, R. Koter, M. Hartelt, D. Spaltmann, S. Pentzien, S. Hoehm, A. Rosenfeld, J. Krüger, Femtosecond laser-induced periodic surface structures on steel and titanium alloy for tribological applications, Appl. Phys. A Mater. Sci. Process. 117 (2014) 103–110, https://doi.org/10.1007/s00339-014-8229-2.
[23] J. Bonse, R. Koter, M. Hartelt, D. Spaltmann, S. Pentzien, S. Höhm, A. Rosenfeld, J. Krüger, Tribological performance of femtosecond laser-induced periodic surface structures on titanium and a high toughness bearing steel, Appl. Surf. Sci. 336 (2015) 21–27, https://doi.org/10.1016/j.apsusc.2014.08.111.
[24] C. Florian, R. Wonneberger, A. Undisz, S.V. Kirner, K. Wasmuth, D. Spaltmann, J. Krüger, J. Bonse, Chemical effects during the formation of various types of femtosecond laser-generated surface structures on titanium alloy, Appl. Phys. A 126 (2020) 1–11, https://doi.org/10.1007/s00339-020-3434-7.
[25] A. Mizuno, T. Honda, J. Kikuchi, Y. Iwai, N. Yasumaru, K. Miyazaki, Friction properties of the DLC film with periodic structures in nano-scale, Tribol. Online 1 (2006) 44–48, https://doi.org/10.2474/trol.1.44.
[26] J. Eichstädt, G.R.B.E. Römer, A.J. Huis, Towards friction control using laser-induced periodic surface structures, Phys. Procedia 12 (2011) 7–15, https://doi.org/10.1016/j.phpro.2011.03.099.
[27] A. Volchok, G. Halperin, I. Etsion, The effect of surface regular microtopography on fretting fatigue life, Wear 253 (2002) 509–515, https://doi.org/10.1016/S0043-1648(02)00148-5.
[28] Y. Choi, J. Lee, A study on the effects of surface dimple geometry on fretting fatigue performance, Int. J. of Precis. Eng. Manuf. 16 (2015) 707–713, https://doi.org/10.1007/s12541-015-0094-1.
[29] Z.R. Zhou, L. Vincent, Mixed fretting regime, Wear 181 (1995) 531–536, https://doi.org/10.1016/0043-1648(95)90168-X.
[30] G. Stachowiak, A.W. Batchelor, Engineering Tribology, Butterworth-heinemann, 2013, https://doi.org/10.1016/C2011-0-07515-4.
[31] J.J. Ayerdi, N. Slachciak, I. Llavori, A. Zabala, A. Aginagalde, J. Bonse, D. Spaltmann, On the role of a ZDDP in the tribological performance of femtosecond laser-induced periodic surface structures on titanium alloy against different counterbody materials, Lubricants 7 (2019) 79, https://doi.org/10.3390/lubricants7090079.
[32] Y. Li, K. Chen, X. Dang, F. Zhang, N. Tamura, C.S. Ku, H. Kang, H.R. Wenk, XtalCAMP: a comprehensive program for the analysis and visualization of scanning Laue X-ray micro−/nanodiffraction data, J. Appl. Cryst. 53 (2020) 1392–1403, https://doi.org/10.1107/S1600576720010882.
[33] J. Bonse, S. Höhm, R. Koter, M. Hartelt, D. Spaltmann, S. Pentzien, A. Rosenfeld, J. Krüger, Tribological performance of sub-100-nm femtosecond laser-induced periodic surface structures on titanium, Appl. Surf. Sci. 374 (2016) 190–196, https://doi.org/10.1016/j.apsusc.2015.11.019.
[34] G. Zhao, G. Wang, Y. Li, L. Wang, Y. Lian, Y. Yu, H. Zhao, Y. Wang, Z. Lu, Femtosecond laser-induced periodic surface structures on hard and brittle materials, Sci. China Technol. Sci. 67 (2024) 19–36, https://doi.org/10.1007/s11431-022-2327-8.
[35] Z. Wang, Q.Z. Zhao, Friction reduction of steel by laser-induced periodic surface nanostructures with atomic layer deposited TiO_2 coating, Surf. Coat. Tech. 344 (2018) 269–275, https://doi.org/10.1016/j.surfcoat.2018.03.036.
[36] G. Schnell, H. Lund, S. Bartling, C. Polley, A. Riaz, V. Senz, H. Seitz, Heat accumulation during femtosecond laser treatment at high repetition rate–a morphological, chemical and crystallographic characterization of self-organized structures on Ti6Al4V, Appl. Surf. Sci. 570 (2021) 151115, https://doi.org/10.1016/j.apsusc.2021.151115.
[37] K. Xiao, M. Li, M. Li, R. Dai, Z. Hou, J. Qiao, Femtosecond laser ablation of AZ31 magnesium alloy under high repetition frequencies, Appl. Surf. Sci. 594 (2022) 153406, https://doi.org/10.1016/j.apsusc.2022.153406.
[38] Q. Yang, H. Zhang, W. Zhou, Surface incubation effect of carbide yg6 induced by femtosecond laser, Acta Photonica Sinica 48 (2019) 614002, https://doi.org/10.3788/gzxb20194806.0614002.
[39] C.A. Zuhlke, T.P. Anderson, D.R. Alexander, Formation of multiscale surface structures on nickel via above surface growth and below surface growth mechanisms using femtosecond laser pulses, Opt. Express 21 (2013) 8460–8473, https://doi.org/10.1364/OE.21.008460.
[40] T. Weikert, S. Wartzack, M.V. Baloglu, K. Willner, S. Gabel, B. Merle, F. Pineda, M. Walczak, M. Marian, A. Rosenkranz, S. Tremmel, Evaluation of the surface fatigue behavior of amorphous carbon coatings through cyclic nanoindentation, Surf. Coat. Technol. 407 (2021) 126769, https://doi.org/10.1016/j.surfcoat.2020.126769.
[41] D.F. Zambrano-Mera, R. Espinoza-González, A. Rosenkranz, T.J. Harvey, T. Polcar, P. Valenzuela, W. Gacitúa, Enhanced erosion resistance of anti-reflective TiO_2/SiO_2 coatings induced by Zr-oxide doping, Sol. Energ. Mat. Sol. C. 250 (2023) 112079, https://doi.org/10.1016/j.solmat.2022.112079.
[42] Y. Yu, L. Zhou, M. Li, Z. Cai, S. Luo, W. He, X. Fang, Research on fretting regime transition of DD6 single-crystal superalloy via femtosecond laser-induced asperity and hardened layer, Appl. Surf. Sci. 610 (2023) 155392, https://doi.org/10.1016/j.apsusc.2022.155392.
[43] L. Kuang, Z. Chen, Y. Jiang, Z. Wang, R. Wang, C. Liu, Adiabatic shear behaviors in rolled and annealed pure titanium subjected to dynamic impact loading, Mater. Sci. Eng. A 685 (2017) 95–106, https://doi.org/10.1016/j.msea.2017.01.011.
[44] G. Zhou, Y. Zhang, W. Pantleon, J. Kou, U. Ramamurty, X. Tan, S. Luo, W. He, C. S. Ku, C.Y. Chiang, N. Tamura, Quantification of room temperature strengthening of laser shock peened Ni-based superalloy using synchrotron microdiffraction, Mater. Des. 221 (2022) 110948, https://doi.org/10.1016/j.matdes.2022.110948.
[45] A. Clair, M. Foucault, O. Calonne, Y. Lacroute, L. Markey, M. Salazar, V. Vignal, E. Finot, Strain mapping near a triple junction in strained Ni-based alloy using EBSD and biaxial nanogauges, Acta Mater. 59 (2011) 3116–3123, https://doi.org/10.1016/j.actamat.2011.01.051.
[46] A.A. Tiamiyu, V. Tari, J.A. Szpunar, A.G. Odeshi, A.K. Khan, Effects of grain refinement on the quasi-static compressive behavior of AISI 321 austenitic stainless steel: EBSD, TEM, and XRD studies, Int. J. Plast. 107 (2018) 79–99, https://doi.org/10.1016/j.ijplas.2018.03.014.
[47] Y.B. Chun, M. Battaini, C.H. Davies, S.K. Hwang, Distribution characteristics of in-grain misorientation axes in cold-rolled commercially pure titanium and their correlation with active slip modes, Metall. Mater. Trans. A 41 (2010) 3473–3487, https://doi.org/10.1007/s11661-010-0410-4.
[48] K. Wang, M. Wu, Z. Yan, D. Li, R. Xin, Q. Liu, Microstructure evolution and static recrystallization during hot rolling and annealing of an equiaxed-structure TC21 titanium alloy, J. Alloys Compd. 752 (2018) 14–22, https://doi.org/10.1016/j.jallcom.2018.04.148.
[49] A. Bisht, R. Kalsar, A. Adak, I. Dey, K. Jana, A. Lad, G.R. Kumar, G. Jagadeesh, S. Suwas, Observation of ex-situ microstructure relaxation of non-conventional misorientations post femtosecond laser shock exposure in cp-Ti, Acta Mater. 150 (2018) 161–172, https://doi.org/10.1016/j.actamat.2018.03.001.
[50] C. Ma, H. Wang, T. Hama, X. Guo, X. Mao, J. Wang, P. Wu, Twinning and detwinning behaviors of commercially pure titanium sheets, Int. J. Plast. 121 (2019) 261–279, https://doi.org/10.1016/j.ijplas.2019.06.010.
[51] S.I. Ashitkov, N.A. Inogamov, V.V. Zhakhovskii, Y.N. Emirov, M.B. Agranat, I. I. Oleinik, S.I. Anisimov, V.E. Fortov, Formation of nanocavities in the surface layer of an aluminum target irradiated by a femtosecond laser pulse, JETP Lett. 95 (2012) 176–181, https://doi.org/10.1134/S0021364012040042.
[52] X. Sedao, A. Abou Saleh, A. Rudenko, T. Douillard, C. Esnouf, S. Reynaud, C. Maurice, F. Pigeon, F. Garrelie, J.P. Colombier, Self-arranged periodic nanovoids by ultrafast laser-induced near-field enhancement, ACS Photonics 5 (2018) 1418–1426, https://doi.org/10.1021/ACSPHOTONICS.7B01438.
[53] A. Rudenko, C. Mauclair, F. Garrelie, R. Stoian, J.P. Colombier, Amplification and regulation of periodic nanostructures in multipulse ultrashort laser-induced surface evolution by electromagnetic-hydrodynamic simulations, Phys. Rev. B 99 (2019) 235412, https://doi.org/10.1103/PHYSREVB.99.235412.
[54] M. Tsujino, T. Sano, T. Ogura, M. Okoshi, N. Inoue, N. Ozaki, R. Kodama, K. F. Kobayashi, A. Hirose, Formation of high-density dislocations and hardening in femtosecond-laser-shocked silicon, Appl. Phys. Express 5 (2012) 022703, https://doi.org/10.1143/APEX.5.022703.
[55] S.I. Ashitkov, N.A. Inogamov, P.S. Komarov, V.V. Zhakhovsky, I.I. Oleynik, M. B. Agranat, G.I. Kanel, V.E. Fortov, Strength of metals in liquid and solid states at extremely high tension produced by femtosecond laser heating, AIP Conf. Proc. 1464 (2012) 120–125, https://doi.org/10.1063/1.4739866.
[56] T. Kawashima, T. Sano, A. Hirose, S. Tsutsumi, K. Masaki, K. Arakawa, H. Hori, Femtosecond laser peening of friction stir welded 7075-T73 aluminum alloys, J. Mater. Process. Technol. 262 (2018) 111–122, https://doi.org/10.1016/j.jmatprotec.2018.06.022.
[57] W.J. Keller, N. Shen, A.M. Rubenchik, S. Ly, R. Negres, R.N. Raman, J.H. Yoo, G. Guss, J.S. Stolken, M.J. Matthews, J.D. Bude, Physics of picosecond pulse laser ablation, J. Appl. Phys. 125 (2019) 085103, https://doi.org/10.1063/1.5080628.
[58] E.I. Ageev, Y.M. Andreeva, A.A. Ionin, N.S. Kashaev, S.I. Kudryashov, N. V. Nikonorov, R.K. Nuryev, A.A. Petrov, A.A. Rudenko, A.A. Samokhvalov, I. N. Saraeva, Single-shot femtosecond laser processing of Al-alloy surface: an interplay between Mbar shock waves, enhanced microhardness, residual stresses, and chemical modification, Opt. Laser Technol. 126 (2020) 106131, https://doi.org/10.1016/j.optlastec.2020.106131.
[59] J. Zhao, K. Wang, K. Huang, G. Liu, Recrystallization behavior during hot tensile deformation of TA15 titanium alloy sheet with substantial prior deformed substructures, Mater Charact 151 (2019) 429–435, https://doi.org/10.1016/j.matchar.2019.03.029.
[60] S. Valette, E. Audouard, R. Le Harzic, N. Huot, P. Laporte, R. Fortunier, Heat affected zone in aluminum single crystals submitted to femtosecond laser irradiations, Appl. Surf. Sci. 239 (2005) 381–386, https://doi.org/10.1016/j.apsusc.2004.06.003.
[61] Y. Yang, H. Zhang, H. Qiao, Microstructure characteristics and formation mechanism of TC17 titanium alloy induced by laser shock processing, J. Alloys Compd. 722 (2017) 509–516, https://doi.org/10.1016/j.jallcom.2017.06.127.

[62] Y.X. Ye, Y.Y. Feng, Z.C. Lian, Y.Q. Hua, Plastic deformation mechanism of polycrystalline copper foil shocked with femtosecond laser, Appl. Surf. Sci. 309 (2014) 240–249, https://doi.org/10.1016/j.apsusc.2014.05.019.
[63] G.Z. Quan, G.C. Luo, J.T. Liang, D.S. Wu, A. Mao, Q. Liu, Modelling for the dynamic recrystallization evolution of Ti–6Al–4V alloy in two-phase temperature range and a wide strain rate range, Comput. Mater. Sci. 97 (2015) 136–147, https://doi.org/10.1016/j.commatsci.2014.10.009.
[64] X. Pan, X. Wang, Z. Tian, W. He, X. Shi, P. Chen, L. Zhou, Effect of dynamic recrystallization on texture orientation and grain refinement of Ti6Al4V titanium alloy subjected to laser shock peening, J. Alloys Compd. 850 (2021) 156672, https://doi.org/10.1016/j.jallcom.2020.156672.
[65] T. Sakai, M.E. Fine, Basal slip of Ti Al single crystals, Scr. Metall. 8 (1974) 545–547, https://doi.org/10.1016/0036-9748(74)90066-0.
[66] A. Akhtar, E. Teghtsoonian, Prismatic slip in α-Ti single crystals, Metall. Trans. A. 6 (1975) 2201–2208, https://doi.org/10.1007/BF02818644.
[67] M. Yoo, Slip, twinning, and fracture in hexagonal close-packed metals, Metall. Trans. A. 12 (1981) 409–418, https://doi.org/10.1007/BF02648537.
[68] C. Zhang, Y. Dong, C. Ye, Recent developments and novel applications of laser shock peening: a review, Adv. Eng. Mater. 23 (2021) 2001216, https://doi.org/10.1002/adem.202001216.
[69] L. Dai, W. Song, A strain rate and temperature-dependent crystal plasticity model for hexagonal close-packed (HCP) materials: application to α-titanium, Int. J. Plast. 154 (2022) 103281, https://doi.org/10.1016/j.ijplas.2022.103281.
[70] H. Sun, J. Li, M. Liu, D. Yang, F. Li, A review of effects of femtosecond laser parameters on metal surface properties, Coatings 12 (2022) 1596, https://doi.org/10.3390/coatings12101596.
[71] Z.R. Zhou, L. Vincent, Effect of external loading on wear maps of aluminium alloys, Wear 162 (1993) 619–623, https://doi.org/10.1016/0043-1648(93)90552-W.
[72] Z.R. Zhou, L. Vincent, Cracking induced by fretting of aluminium alloys, J. Tribol. 119 (1997) 36–42, https://doi.org/10.1115/1.2832477.
[73] B. Zhao, Y. Zhang, Y. Fan, X. Yu, Z. Zhang, B. Zhang, The three-body abrasive tribological characteristics of the graphene/h-BN heterostructure film considering defects, Tribol. Int. 171 (2022) 107525, https://doi.org/10.1016/j.triboint.2022.107525.
[74] M.H. Zhu, X.Q. Fan, Z.B. Cai, J.F. Peng, Q. Sun, Surface engineering design on alleviating fretting wear: a review, Surf. Sci. Technol. 1 (2023) 4, https://doi.org/10.1007/s44251-023-00003-8.
[75] J. Hu, H. Song, S. Sandfeld, X. Liu, Y. Wei, Breakdown of Archard law due to transition of wear mechanism from plasticity to fracture, Tribol. Int. 173 (2022) 107660, https://doi.org/10.1016/j.triboint.2022.107660.
[76] X. Li, Y. Guan, Theoretical fundamentals of short pulse laser–metal interaction: a review, Nanotech. Precis. Eng. 3 (2020) 105–125, https://doi.org/10.1016/j.npe.2020.08.001.